SKB

SSRT testing of copper in sulfide solutions

Alice Moya Núñez

Claes Taxén

SVENSK KÄRNBRÄNSLEHANTERING

SSRT testing of copper in sulfide solutions

Alice Moya Núñez, Claes Taxén

RISE Research Institutes of Sweden AB

Summary

Copper is the intended canister material for the disposal of spent nuclear fuel in Sweden. At repository depth the groundwater may contain dissolved sulfide. The main goal for this work is to study the tendency for stress corrosion of copper in sulfide solutions and examine the influence of various experimental parameters on stress corrosion.

Slow strain rate testing was performed on copper test rods in solutions with 1.0 mM sulfide. The pH was kept near neutral with phosphate or borate buffer. This investigation expands the test matrix of a previous study conducted during 2018–2019 and the test matrix included variations in temperature, strain rate, duration of the tests as well salt and buffer concentrations. In the present study, test rods were strained up to about 20 % (14 % in one test) and then the tests were interrupted. Cross sections of the specimens after test were investigated using SEM/EDS. As before, the stress strain curves do not reveal any signs of stress corrosion. However, intergranular corrosion in the shape of crack and pit-like features developed in all tests with 1.0 mM sulfide. The length of the deepest features in all these tests was of the same order of magnitude (10–20 μm).

The suggested mechanism proposes that crack-like features originate at the surface of the copper metal from the oxidation of grain boundaries that behave as slightly less noble than grain bodies. Neighbouring grains are pulled apart by strain as the common boundary corrodes. The resulting cavity is then slowly filled with solid copper sulfide thus restricting the diffusion between bare metal sites in the cavity and the bulk solution. Propagation of such a local attack stops when there is no longer any open path for the corrodent HS^- to reach any bare metal site in the cavity.

Contents

1 Introduction

In a previous study during 2019, copper rods were tested for signs of stress corrosion cracking (SCC) in 1 mM sulfide solutions at 30, 60 and 90 °C with an extension rate of 5×10^{-6} s^{-1} (Taxén et al. 2019). During this investigation, no signs of SCC were detected in the recorded strain/stress curves. A small number of crack-like features was found after cross-section analysis. The initiation and subsequent propagation of the crack-like features was explained through the hypothesis of intergranular corrosion aggravated by strain.

In the present work some selected conditions are equivalent to those in 2019, with the addition of a few variations with the aim to expand the test matrix. The main goal is to study the influence of various test parameters on the tendency for SCC of copper in sulfide solutions.

The mechanism to test proposes that crack-like features originate at the surface of the copper metal from the oxidation of grain boundaries that behave as slightly less noble than grain bodies. Neighbouring grains are pulled apart by strain as the common boundary corrodes. The resulting cavity is then slowly filled with solid copper sulfide thus restricting the diffusion between bare metal sites in the cavity and the bulk solution. Propagation of such a local attack stops when there is no longer any open path for the corrodent HS$^-$ to reach any bare metal site in the cavity.

2 Experimental

2.1 Material

2.1.1 Specimens

The specimens for this run were produced following the same procedure described in the published report TR-19-13 (Taxén et al. 2019).

The copper material was supplied by SKB and cut from lid TX#219. Test rods were cut from the base material by spark cutting followed by turning on a lathe. The test rods were fully annealed by treatment in molten salt at 600 °C for 10 minutes and quenching in water for about 60 s or until the test rod could be touched by hand. Any remaining traces of salt were carefully removed from the whole test rod using P320 grit paper in a lathe at slow speed. The final grinding of the middle section of the test rod, the section that was exposed to the solution, was with P600 grit paper, also in a lathe. The rods were then degreased using ethanol and rinsed in deionized water immediately before mounting in the SSRT cell. Figure 2-1 shows a sketch of the dimensions for the test rods.
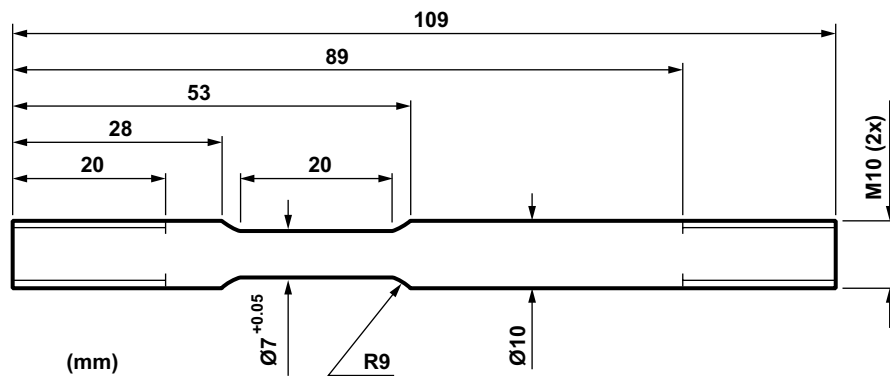

Figure 2-1. *Drawing of test rods. Measurements in mm.*

2.1.2 Specimen preparation procedure for SEM

The rods were removed from the SSRT machine and cut in half longitudinally using a high speed precision saw (Struers Accutom-50). Before cutting, the surface of the rods was examined using Light Optical Microscopy (LOM) and Scanning Electron Microscopy (SEM). One half of each specimen was mounted in a conductive thermoset material (KonductoMet). The mounted cross sections were then ground successively to paper grit P4000 and polished using a SiO_2 suspension.

The cross sections of the specimens were examined using a SEM (Zeiss Gemini 450) equipped with chemical analysis by Energy Dispersive X-Ray Spectroscopy (EDS). The software AZtec by Oxford Instruments was used for the EDS analysis.

All the features along the narrow section were recorded, whether they had "pit" or "crack-like" appearance. The lengths of the features were measured directly from the SEM images using the image processing software ImageJ (Schneider et al. 2012), and were taken as a straight line from the feature's surface to its end, following its shape.

2.1.3 Specimen preparation procedure for FIB/TEM

The experimental details for the FIB/TEM procedure are described in Appendix A.

2.2 Flow system

The experimental setup used was equivalent to the one used in the previous study (Taxén et al. 2019). As in the previous study, two stock solutions were fed by a tube pump. The alkaline sulfide stock solution was mixed with the buffer solution in the SSRT-cell. The tube pump ensured that the two solutions were fed at the same rate. Figure 2-2 illustrates the experimental setup. Phosphate buffer solutions were generally used in the present study, with the exception of one run which used a borate-containing solution.
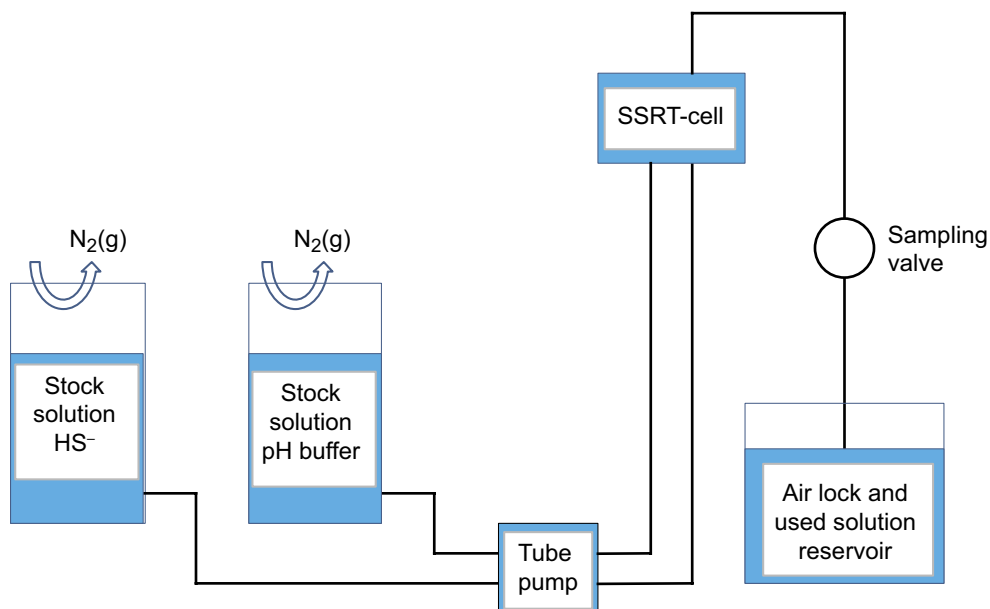
Figure 2-2. *Schematic sketch of the solution flow system during SSRT-test of copper.*

2.3 Stock solutions

Both stock solutions contained NaCl at the selected concentration. Na_2S was added to one of the stock solutions and a weighed amount of NaOH(s) to the other which was subsequently neutralized by either phosphoric acid (H_3PO_4) or boric acid (H_3BO_3) to pH 7.2. The concentrations of the acids were only approximate, whereas the amount of sodium could be added with greater precision and neutralisation of the excess hydroxide gave the desired buffer concentration. Batches of 10 liters were prepared and for the slower strain test which lasted about 14 days, the stock solution vessels were refilled once for that case. The pH concentration of the solution was measured using pH meters from Metrohm, model 691, and from Jenaway, model 3220. The corrosion potentials of the specimens were measured using a Fluke f79 True RMS Multimeter.

2.3.1 Characteristics of the test solutions

Table 2-1 shows the contents of the main species in test solutions together with calculated values for the ionic strengths and the electrolytic conductivity at 25 °C. Diffusion coefficients are taken from (Lide 2002–2003). No reliable value for the boric compounds were found and a value judged to be reasonable from previous experience was used. The effect on the estimated conductivity of solution C should be minor.

Ionic conductivity was calculated from the sum of the contributions of each species at infinite dilution. Each contribution was calculated from the concentration multiplied by the limiting molar conductivity, λ_i, for the ion, i, according to Nernst-Einsteins' equation (Birks et al. 2006):

$$\lambda_i = \frac{F^2}{RT} z_i^2 D_i \tag{2-1}$$

F is Faraday's constant, R is the molar gas constant, T is the absolute temperature, z_i is the charge of the ion i and D is the diffusion coefficient.

The ionic strength I was calculated as:

$$I = \frac{1}{2} \Sigma C_i z_i^2 \tag{2-2}$$

C_i is the concentration of the specie i.

Table 2-1. Characteristics of the test solutions, here called *A*, *B* and *C*, respectively.

Specie	Diffusion Coefficient, $D \times 10^9$ (m^2/s)	Charge z	Solution *A* (mM)	Solution *B* (mM)	Solution *C* (mM)
Na^+	1.33	1	27	4.5	13
Cl^-	2.03	−1	10	1	10
$H_2PO_4^-$	0.76	−1	5	0.5	0
HPO_4^{2-}	0.96	−2	5	0.5	0
HS^-	1.73	−1	1	1	1
$B(OH)_4^-$	1.00	−1	0	0	1
$B(OH)_3(aq)$	1.00		0	0	9
Ionic Strength (M)			0.063	0.009	0.025
Ionic Conductivity at 25 °C (S/m)			0.30	0.05	0.15
Buffer Capacity at pH 7.2 (mM/pH)			6	0.6	0.2

Solution *A* is made up of 10 mM NaCl and 10 mM phosphate at pH of about 7.2 with Na^+ as counterion and 2 mM units Na^+ come from the sulfide which is added to the stock solution as Na_2S. The dominating forms of phosphate are $H_2PO_4^-$ and HPO_4^{2-} with about equal concentrations. The total Na^+ concentration is $10 + 2 \times 5 + 5 + 2 \times 1 = 27$ mM.

Solution *B* is ten times more dilute than solution *A*, but has the same sulfide concentration. Solution C has the same NaCl content as Solution *A*. The 10 mM borate buffer in Solution *C* is approximated as being 90 % $B(OH)_3(aq)$ and 10 % $B(OH)_4^-$ at the relevant pH.

One major difference between the solutions is the buffer capacity at pH 7.2. This was calculated for dilute solutions at 25 °C (Stumm and Morgan 1981). Table 2-1 shows that solution *B* has a tenth of the buffer capacity of solution *A* and that solution *C* has the lowest buffer capacity. Borate has a maximum buffer capacity at about pH 9.3 whereas phosphate has a maximum at about pH 7.2 in dilute solutions at 25 °C. For Solution *B*, the pH of the buffer solution was first adjusted to about 7.2 and then spiked with 2 mM HCl in order to counter the alkalizing effect of the sulfide solution.

2.3.2 Procedure

The test cell was first filled with only the buffer solution at ambient temperature. Heating was then applied. The sulfide flow valve was opened when the temperature reached the intended value. Strain was started when the sulfide level, as measured in the drain, had stabilized. For Rod #4 with the low buffer concentration (solution B) which was spiked with acid to counter the high pH of the sulfide solution, a special procedure was adopted. The test cell was filled with the buffer solution before adding the acid. The buffer flow was interrupted, and acid added to the buffer stock solution. Flow of buffer stock solution and sulfide stock solution was started simultaneously.

2.4 Slow strain rate testing

The SSRT test equipment provides data for the applied force (*F*) and for displacement Δy. Engineering stress (σ) and strain (ε) are thus calculated using the following equations:

$$\sigma = \frac{F}{A_m}$$
(2-3)

$$\varepsilon = \frac{\Delta y}{L_a}$$
(2-4)

The average cross sectional area (A_m) is calculated from 5 measurements of the diameter (d_m) of the narrow part of the rod. The active length (L_a) is measured as the distance between the points where the diameter exceeds the average value $d_m + 0.1$ mm at each end of the narrow section.

2.5 Test matrix

Six tests were performed. Table 2-2 shows a summary of the test conditions.

Table 2-2. Summary of the test conditions.

Rod	Temperature (°C)	Sulfide concentration (mM)	(mg/L)	Chloride concentration (mM)	Duration (days)	Strain rate (s⁻¹)	Remarks
#1 (2021.1)	60	1	32	10	14	1×10^{-7}	Solution *A*
#2 (2021.2)	30	1	32	10	4	5×10^{-7}	Solution *A*
#3 (2021.3)	60	1	32	10	4	5×10^{-7}	Finely ground rod (grit 4000) Solution *A*
#4 (2021.4)	60	1	32	1	4	5×10^{-7}	Solution *B*
#5 (2021.5)	75	1	32	10	4	5×10^{-7}	Solution *A*
#6 (2021.6)	60	1	32	10	4	5×10^{-7}	Solution *C*

All the test rods were unloaded after 14 or 4 days by reversing the SSRT machine so that the strain was reduced by the same rate until the test rod could be removed.

2.6 Deviations from the plan/Reproducibility test

Prior to the experiments referred to in the test matrix in Table 2-2, a similar set of experiments was performed during the year 2019 (see Table 2-3). The experiments were started using an unopened can of Na_2S (Sigma-Aldrich) and a new batch of test rods. The same experimental procedure as the one described in our previous work was followed (Taxén et al. 2019). It was however observed that the measured sulfide concentrations were lower than expected and that barely any crack-like features could be seen in the test rods after exposure. The apparent problem with reproducibility was eventually identified as being due to a defect in the batch of the chemical Na_2S. The pH measurements using the defective batch of chemical with respect to a brand new can yielded a difference of about 0.6 pH units.

A new can of Na_2S (Sigma-Aldrich, purchased February 2021) was ordered and tested with respect to sulfide concentration and pH of the prepared solutions. The results of the experimental matrix in Table 2-3 were discarded as being flawed by the defective Na_2S. The new can of Na_2S was handled in N_2 atmosphere and the pH was periodically checked before every run. Before Rod #5 (2021.5), yet another new can of N_2S was purchased (Sigma-Aldrich, purchased September 2021) as the pre-test yielded slightly lower sulfide concentrations, and was used for Rod #5 (2021.5) and Rod #6 (2021.6).

Table 2-3. Summary of the experimental set performed during 2019.

Rod	Temperature (°C)	Sulfide concentration (mM)	(mg/L)	Chloride concentration (mM)	Duration (days)	Strain rate (s⁻¹)	Remarks
2019.1	60	1	32	10	14	1×10^{-7}	
2019.2	30	1	32	10	4	5×10^{-7}	
2019.3	60	1	32	10	4	5×10^{-7}	Finely ground rod (grit P4000)
2019.4	60	1	32	1	4	5×10^{-7}	1 mM phosphate buffer
2019.5	90	1	32	10	4	5×10^{-7}	
2019.6	60	1	32	10	4	5×10^{-7}	

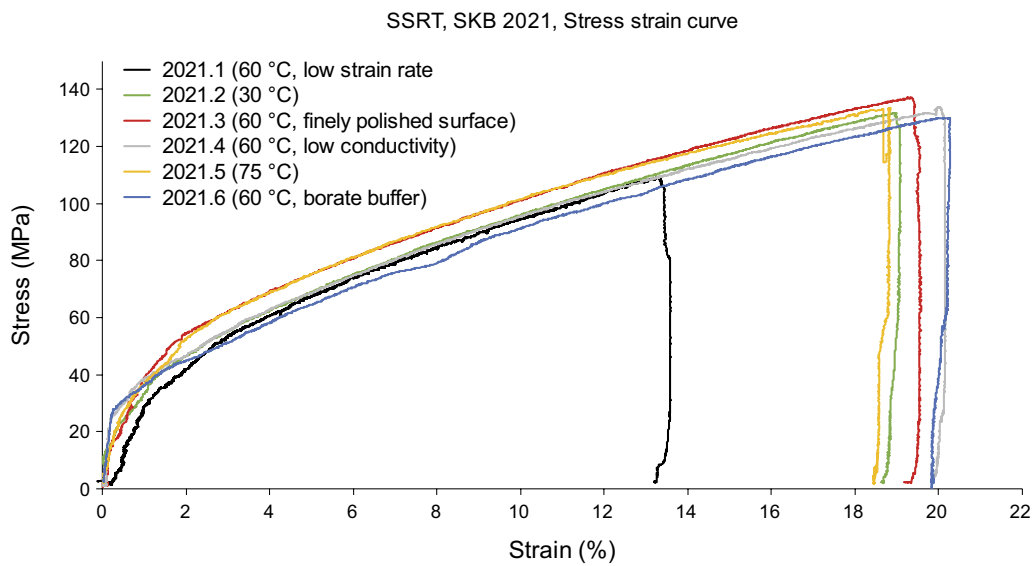# 3 Results

3.1 Stress/strain curves

Figure 3-1 shows the stress/strain curves for copper in near neutral solutions with sulfide and chloride. The strain rate for each experiment was set to either 5×10^{-7} s^{-1} or 1×10^{-7} s^{-1}. The maximum stress in each rod was measured as a result of the set strain rate. This measured stress was slightly lower for two tests: 2021.4 (60 °C, strain rate 5×10^{-7} s^{-1}, low conductivity) and 2021.6 (60°, strain rate 5×10^{-7} s^{-1}, borate buffer). After 4 days of testing at 5×10^{-7} s^{-1} rate, the strain reached an average of 19.5 %. After 4 days of test (14 days for the case of the low rate strain 1×10^{-7} s^{-1}), the stress was gradually decreased and the SSRT machine was reversed. As Figure 3-1 shows, there is still a positive stress indicating an elastic component that is estimated to 0.1–0.2 % strain. The stress/strain curves show results in line with the ones reported in the previous study (Taxén et al. 2019).

Figure 3-1. SSRT stress/strain curves for copper in near neutral solutions with sulfide and chloride.

3.2 Corrosion potentials

Figure 3-2 shows the corrosion potential for the copper test rods and the potential for a platinum wire in the same solution. The corrosion potentials for all tests rods are about −850 mV SCE (saturated calomel electrode). The Pt-potentials are about 450 mV more positive than the corrosion potentials of copper, with the exception of both borate buffer Rod #6 (2021.6) and low conductivity Rod #4 (2021.4) runs, which were about 520 mV more positive. All test rods turned black after exposure.
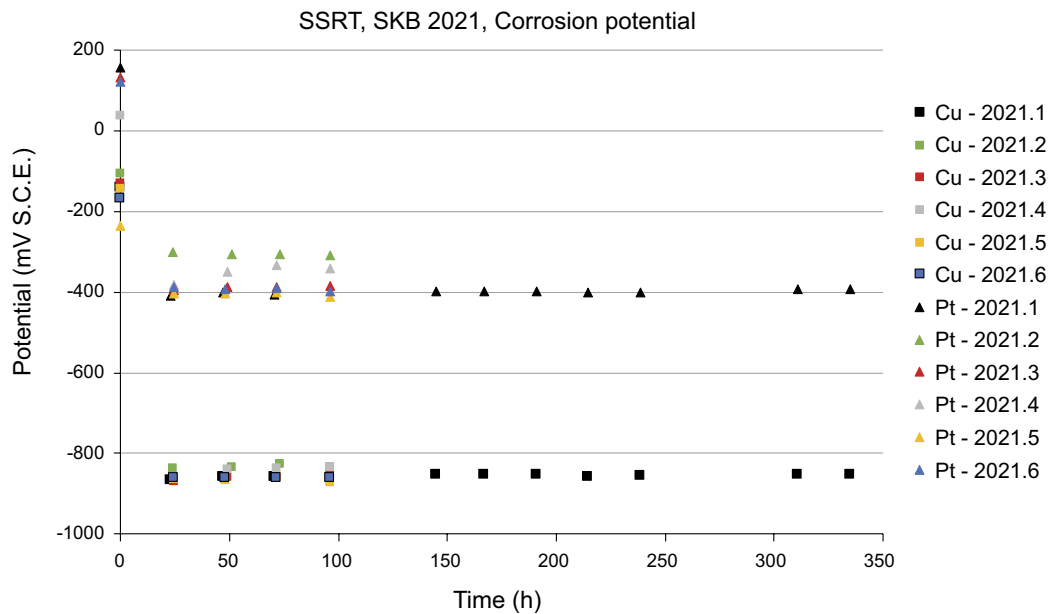
Figure 3-2. *Corrosion potential for copper in near neutral solutions with sulfide and chloride (SCE electrode). The corrosion potential for the copper test rods (square marker) and for platinum wire (triangle marker) in the same solution are shown in the graph.*

3.3 Sulfide concentration

Figure 3-3: Rod #1 (2021.1, 14-day exposure) was refilled once, as shown in the dip occurring at approximately 166 hours.

3.4 pH measurements

Figure 3-4 shows the measured pH in solution from the cell. There were slight variations in pH during the experiments. The solution in Rod #6 (2021.6) was the only one containing borate as buffer, and had a pH of approximately 8.2. The borate pH-buffer solution (solution *C*) had the lowest buffer capacity of the three tested solutions.
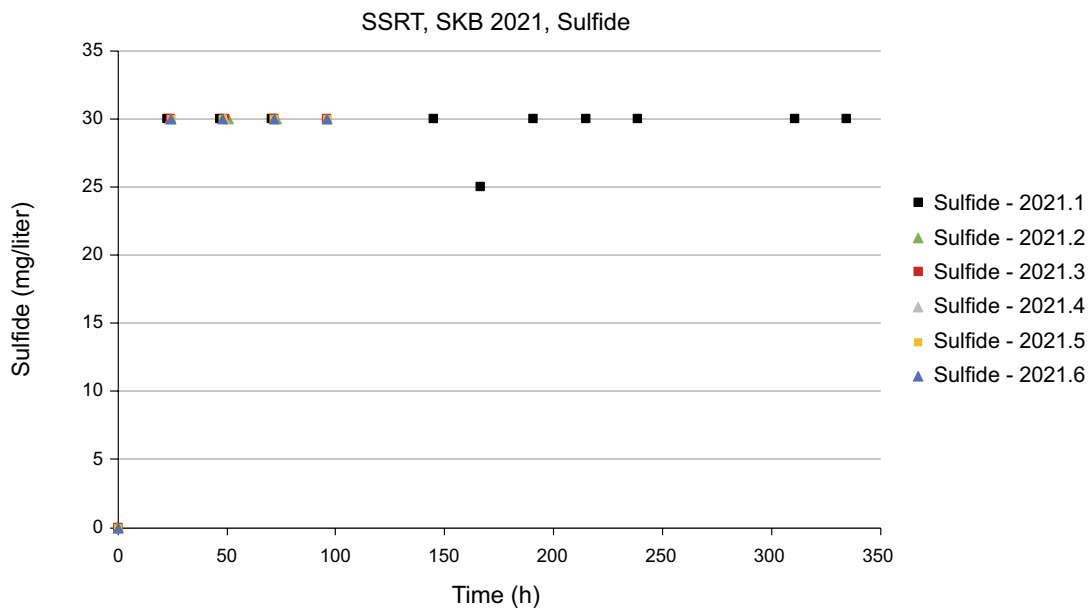

Figure 3-3. *Sulfide concentration for copper in near neutral solutions with sulfide and chloride.*
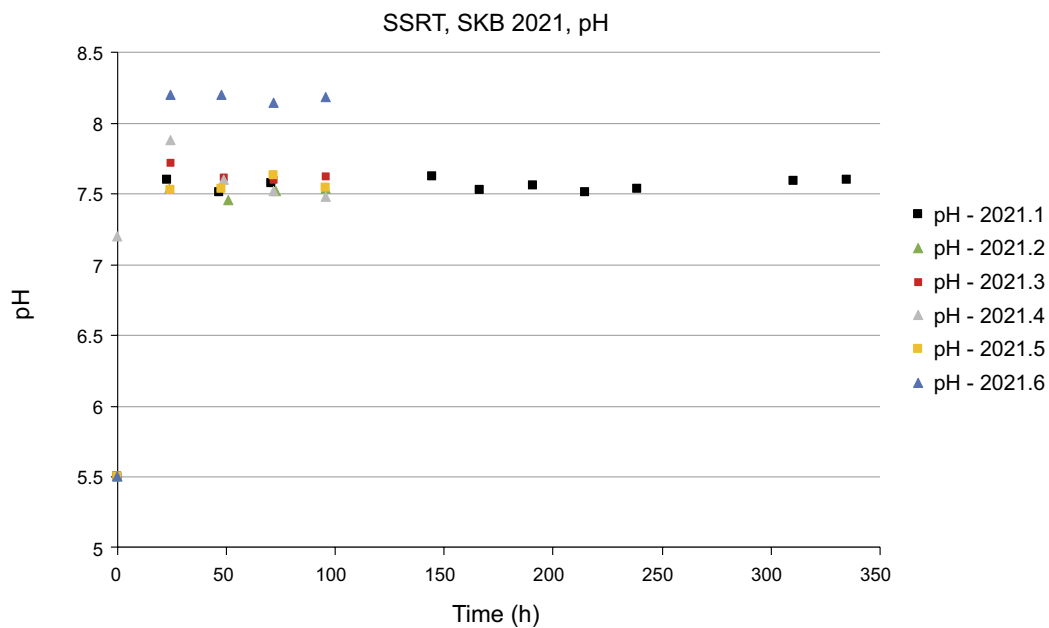

Figure 3-4. *Measured pH in the solutions from the cell.*

3.5 Metallographic examinations – Surfaces

Images from the surfaces of the test rods were taken using LOM and SEM. EDS analysis in selected surfaces was also performed. All of the rods exhibited a black surface after the tests.

3.5.1 Rod #1 (2021.1), 60 °C, low strain rate

Figure 3-5 shows a LOM image of the test Rod #1 (2021.1). The image shows a relatively homogeneous black surface along the rod, although the surface has a metallic sheen. Figure 3-6 shows SEM images of the surface of the rod. The left image shows the lines from the grinding process and the corrosion products formed on top of the surface, containing mainly Cu, S and O. The right image shows a few corrosion product crystals which were identified by EDS as containing mainly Cu and S elements (see Figure 3-7).

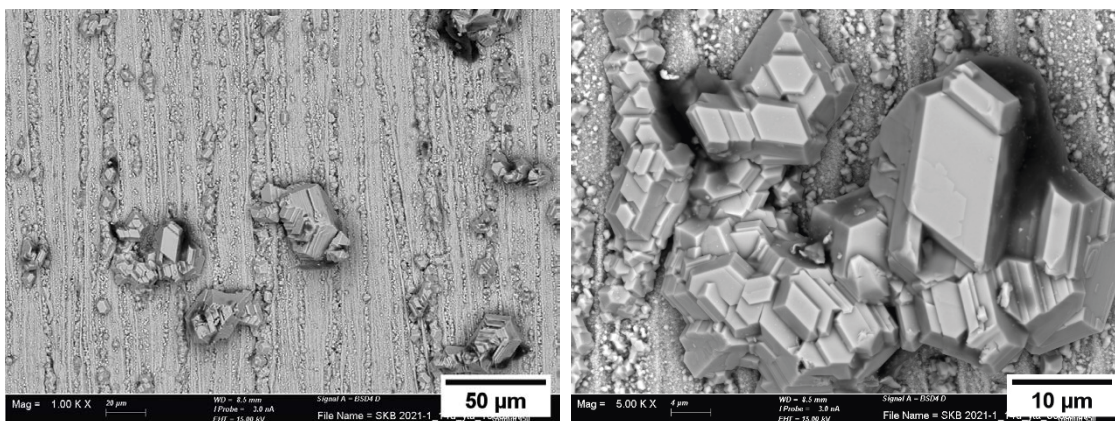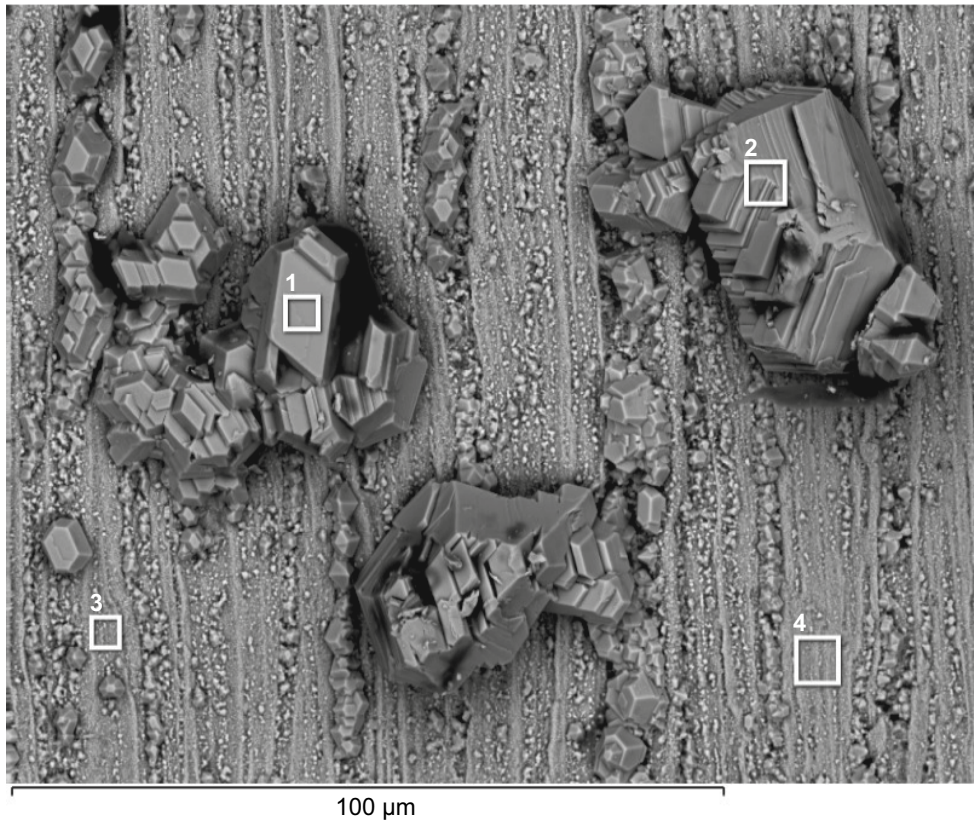***Figure 3-5.*** *LOM image of test Rod #1 (2021.1).*

Figure 3-6. *SEM images of test Rod #1 (2021.1) (BSD mode, 15 kV). Grind lines from specimen preparation and corrosion products are shown in both images.*
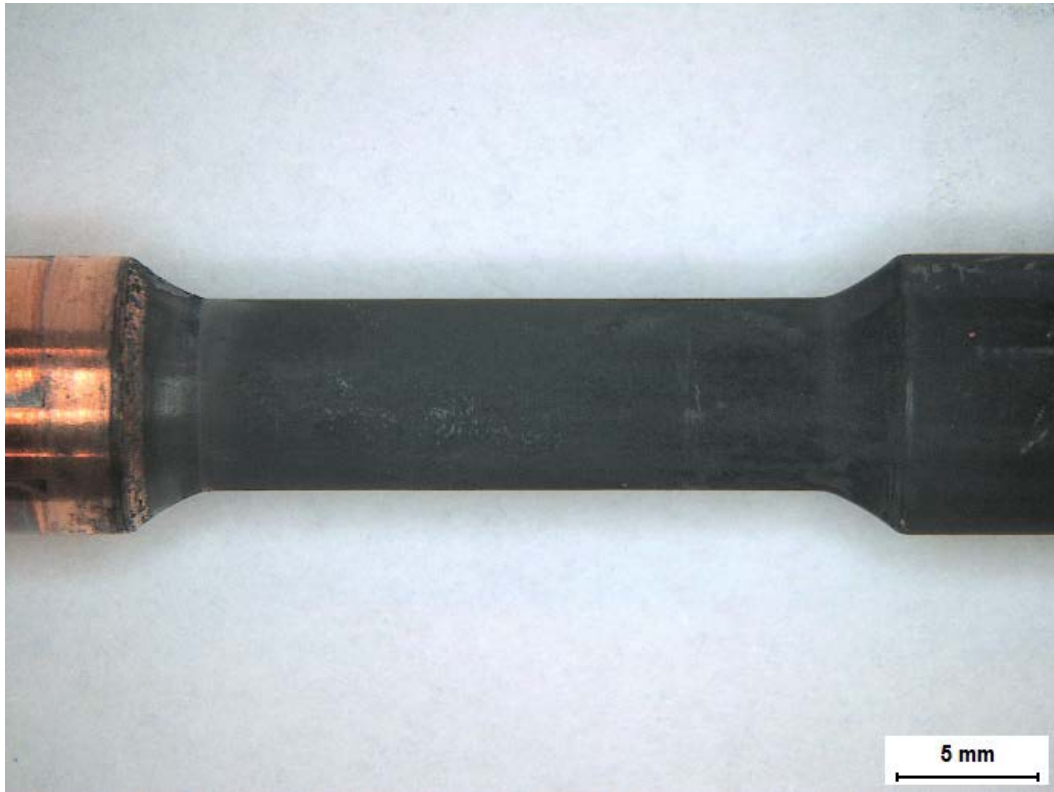
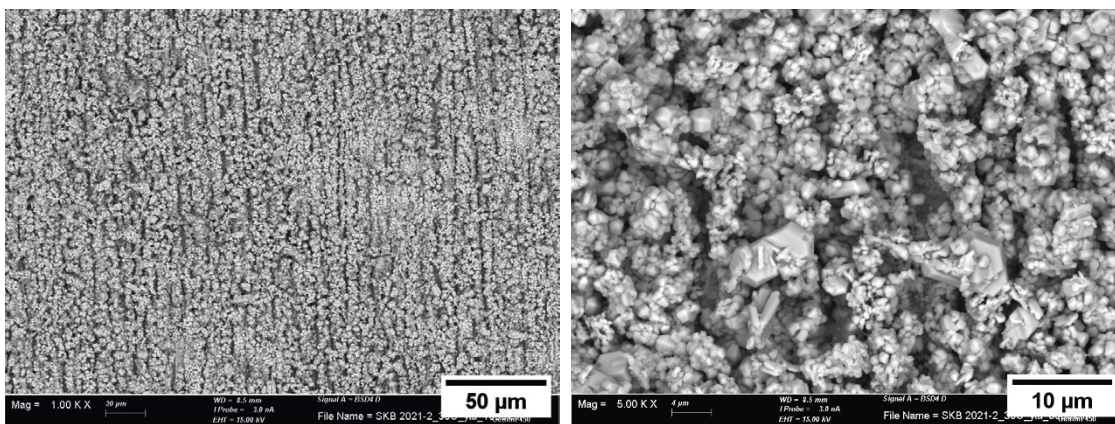| Spectrum label	O	Si	S	Cl	K	Cu	Total
1	1.51	0.26	33.64			64.59	100.00
2	2.87	0.34	32.64			64.15	100.00
3	3.91	0.58	32.89	0.22	0.13	62.27	100.00
4	3.77	0.64	31.92	0.20	0.23	63.24	100.00

Figure 3-7. *SEM image and EDS analysis of the test Rod #1 (2021.1). The location of the areas shown in the image correspond to the spectrum labels in the table. The element analysis by EDS is shown in atomic percent. The location of trace amounts of Cl and K in the surface of the exposed rod (i.e. only in areas where the corrosion layer is thinner, as in spectrum 3 and 4) suggests they do not originate from the test solution, but rather from the pre-exposed copper rod surface.*

3.5.2   Rod #2 (2021.2), 30 °C

Figure 3-8 shows a LOM image of the test Rod #2 (2021.2). The image shows a relatively homogenous black and matte surface along the rod. Figure 3-9 shows SEM images of the surface of the rod. The left image shows the grind lines from the grinding process. The right image shows a few corrosion products crystals which were identified by EDS containing mostly Cu and S elements (see Figure 3-10). The crystals are significantly smaller than in Rod #1 (2021.1) and exhibit a homogenous distribution.

Figure 3-8. *LOM image of test Rod #2 (2021.2).*

Figure 3-9. *SEM images of test Rod #2 (2021.2) (BSD mode, 15 kV). Grind lines from specimen preparation and corrosion products are shown on the surface.*

10 μm
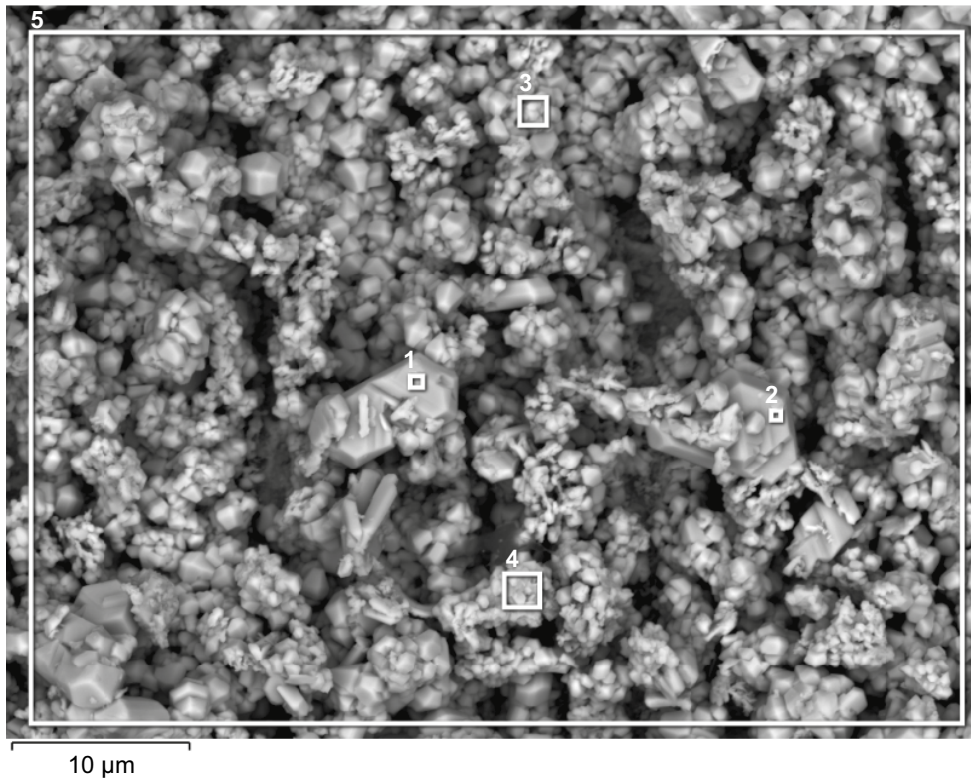
Spectrum label	O	Si	S	Cu	Total
1	0.97	0.29	30.22	68.53	100.00
2	0.95	0.21	31.05	67.78	100.00
3	1.10	0.26	30.62	68.01	100.00
4	1.16	0.26	31.45	67.14	100.00
5	1.50	0.18	31.51	66.81	100.00

Figure 3-10. *SEM image and EDS analysis of the test Rod #2 (2021.2). The location of the areas shown in the image correspond to the spectrum labels in the table. The element analysis by EDS is shown in atomic percent.*

3.5.3 Rod #3 (2021.3), 60 °C, finely polished

Figure 3-11 shows a LOM image of the test Rod #3 (2021.3). The image shows a relatively homogeneous black surface along the rod, retaining a slight metallic sheen. Figure 3-12 shows SEM images of the surface of the rod. The images show corrosion products in the form of a scale with compact appearance and crystals. The EDS analysis shows that both areas are composed primarily of Cu and S elements.
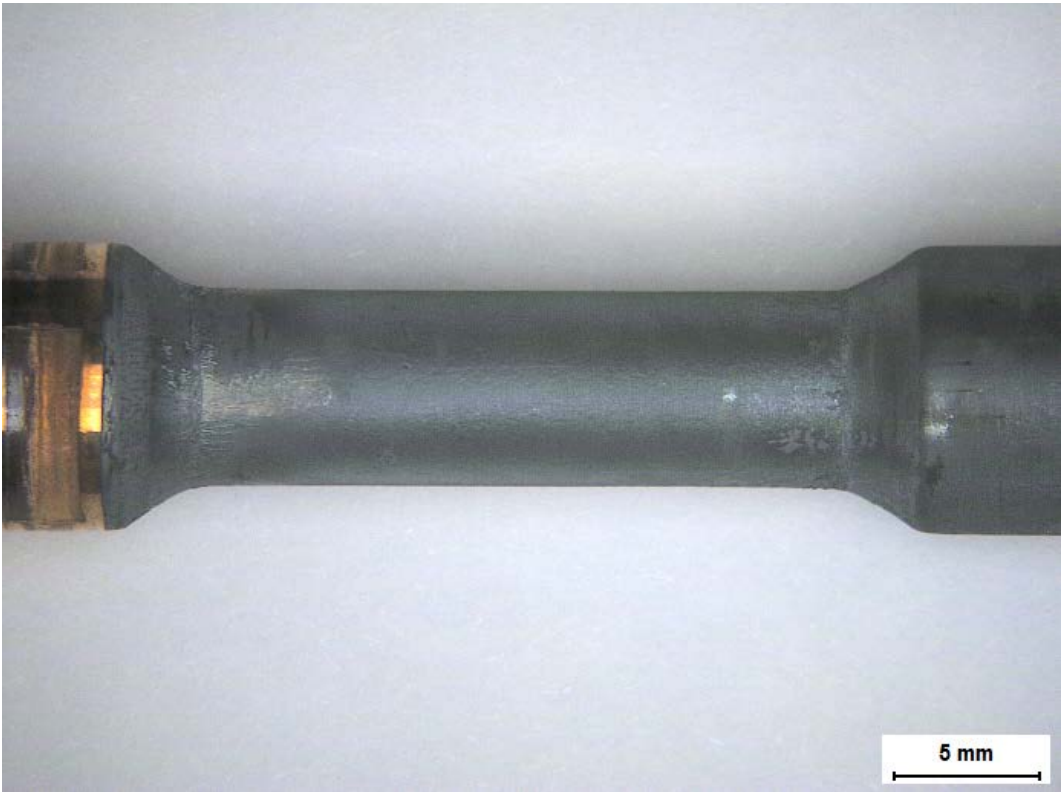

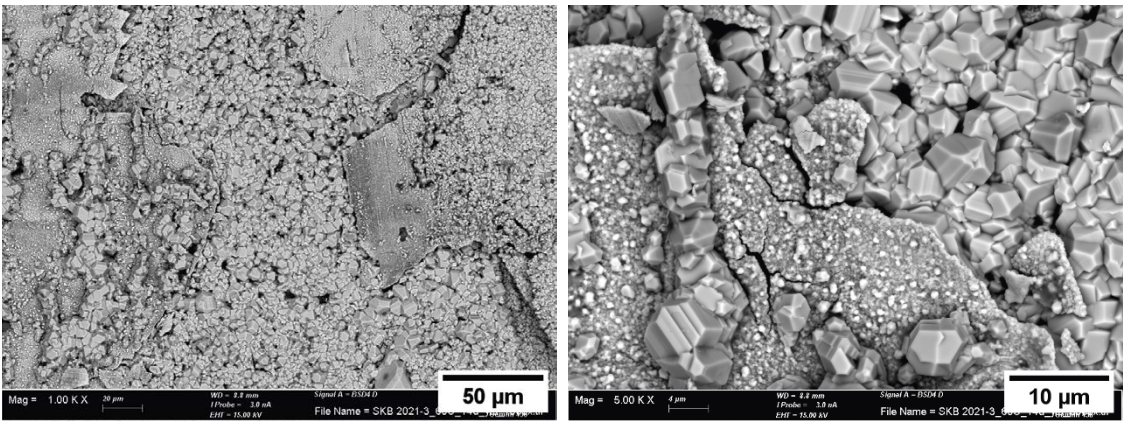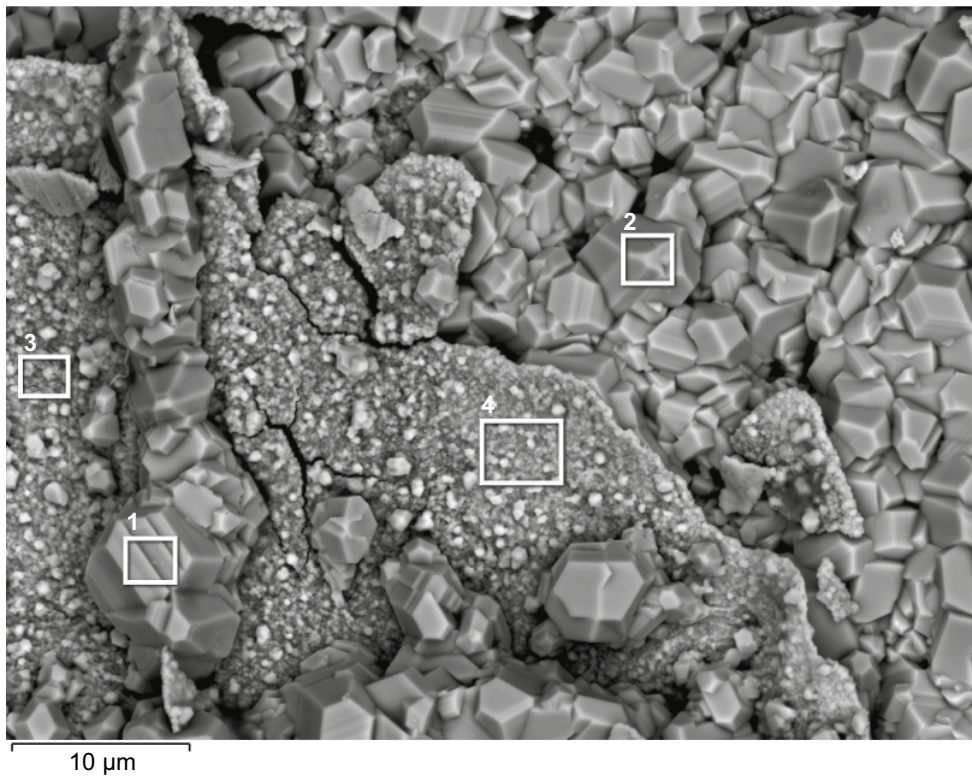*Figure 3-11.* *LOM image of test Rod #3 (2021.3).*

Figure 3-12. *SEM images of test Rod #3 (2021.3) (BSD mode, 15 kV). Both images show corrosion products in form of scale and crystals.*

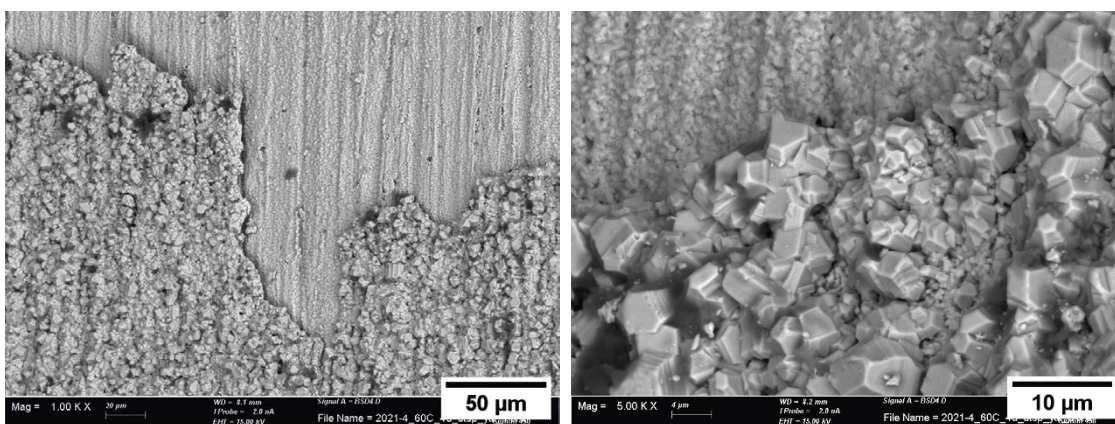| Spectrum label	O	Si	S	Cl	K	Cu	Total
1	2.28	0.30	29.53			67.89	100.00
2	2.31	0.23	30.38			67.07	100.00
3	4.36	0.34	29.57	0.69	0.62	64.41	100.00
4	3.19	0.26	31.33			65.22	100.00

Figure 3-13. *SEM image and EDS analysis of the test Rod #3 (2021.3). The location of the areas shown in the image correspond to the spectrum labels in the table. The element analysis by EDS is shown in atomic percent. The location of trace amounts of Cl and K in the surface of the exposed rod suggests they do not originate from the test solution, but rather from the pre-exposed copper rod surface.*

### 3.5.4 Rod #4 (2021.4), 60 °C, 1 mM phosphate buffer + 1 mM chloride

Figure 3-14 shows a LOM image of the test Rod #4 (2021.4). The image shows a black surface slightly inhomogeneous compared to the other rods. A small area in the top left of the narrow section shows a completely detached scale from the metallic copper surface. Figure 3-15 shows SEM images of the surface of the rod. The images show a two-layered scale; a fine scale underneath and larger crystals resting on top. The EDS analysis shows that both areas are composed primarily of Cu and S elements.

Figure 3-14. *LOM image of test Rod #4 (2021.4).*

Figure 3-15. *SEM images of test Rod #4 (2021.4) (BSD mode, 15 kV). Left image shows grind lines in some areas where the scale has most likely detached. The right image shows a magnification of the scale, composed of crystals.*
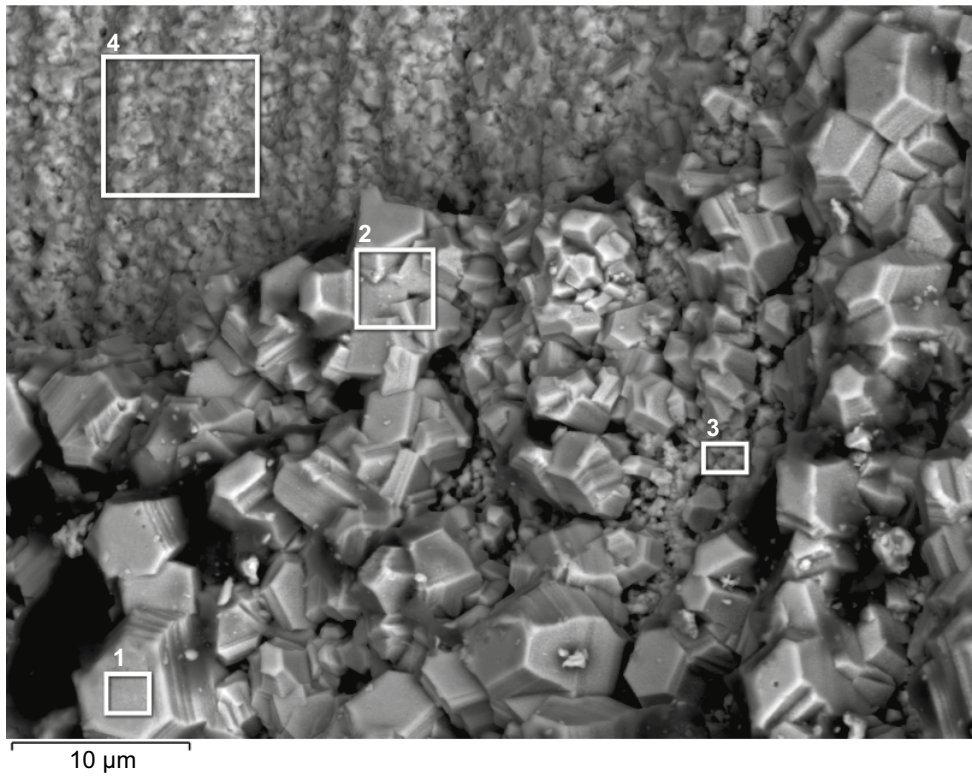
| Spectrum label	O	Si	S	Cu	Total
1	4.31	0.31	31.40	63.97	100.00
2	8.48	0.63	29.27	61.63	100.00
3	8.33	0.23	28.26	63.18	100.00
4	3.08	0.44	31.07	65.42	100.00

Figure 3-16. SEM image and EDS analysis of the test Rod #4 (2021.4). The location of the areas shown in the image correspond to the spectrum labels in the table. The element analysis by EDS is shown in atomic percent.

3.5.5 Rod #5 (2021.5), 75 °C

Figure 3-17 shows a LOM image of the test Rod #5 (2021.5). The image shows a black surface with a slight metallic sheen. Figure 3-18 show SEM images of the surface of the rod. The images show corrosion products in form of crystals following the grind lines from specimen preparation. The crystals tend to accumulate more sharply in some rows. Beneath the crystals there is another scale with finer appearance. The EDS analysis shows that both areas are composed primarily of Cu and S elements (see Figure 3-19).

Figure 3-17. *LOM image of test Rod #5 (2021.5).*
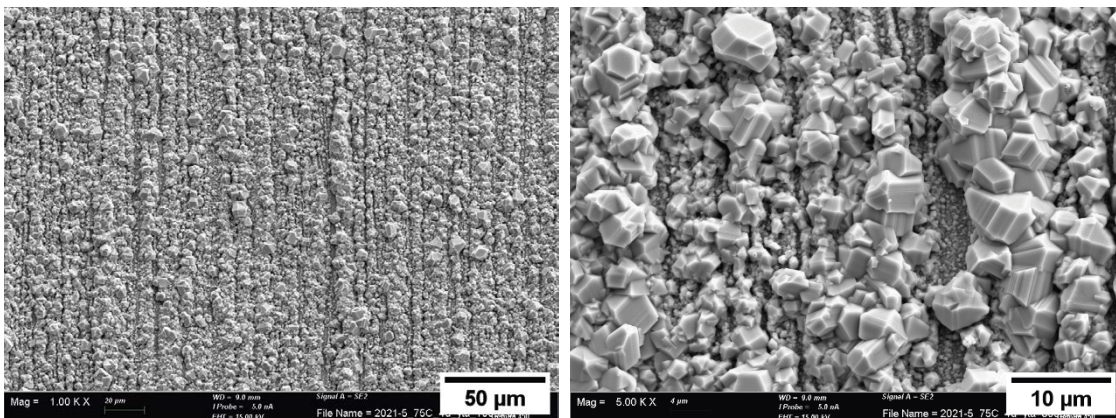
Figure 3-18. *SEM images of test Rod #5 (2021.5) (SE mode, 15 kV). Left image shows grind lines from grinding and corrosion products following said lines. The right image shows a magnification of the corrosion products, which are of crystalline form.*
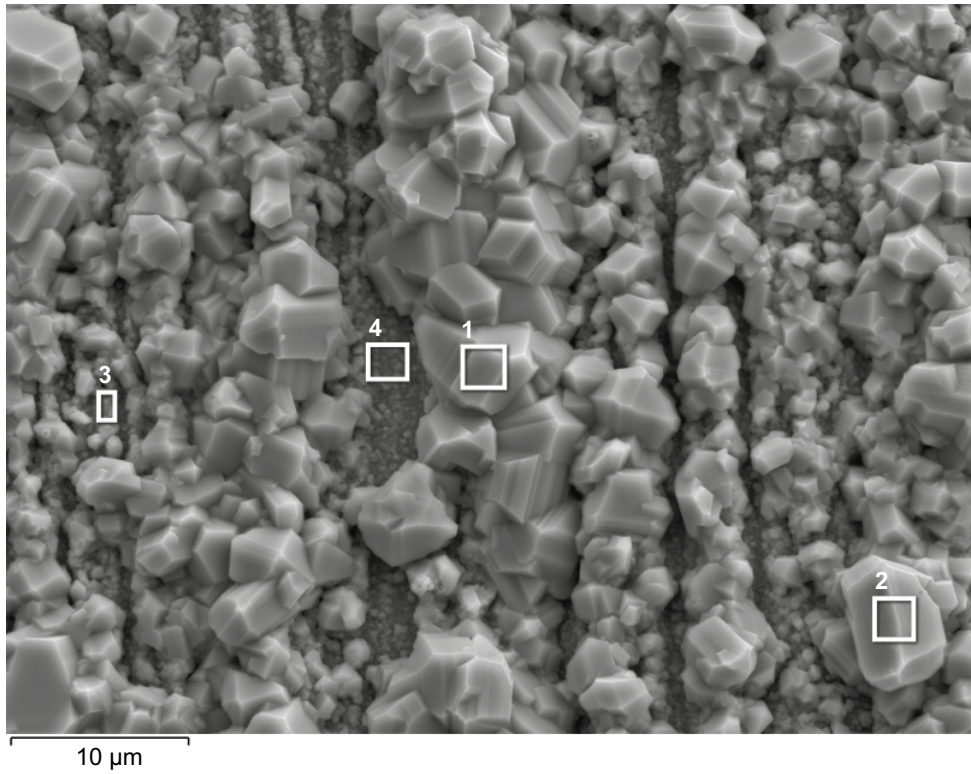
| Spectrum label	O	Si	S	Cu	Total
1	3.59	0.18	31.49	64.73	100.00
2	4.05	0.20	30.81	64.94	100.00
3	2.29	0.39	25.36	71.96	100.00
4	1.56	0.19	19.97	78.28	100.00

Figure 3-19. *SEM image and EDS analysis of the test Rod #5 (2021.5). The location of the areas shown in the image correspond to the spectrum labels in the table. The element analysis by EDS is shown in atomic percent.*

### 3.5.6   Rod #6 (2021.6), 60 °C, borate buffer

Figure 3-20 shows a LOM image of the test Rod #6 (2021.6). The image shows a matte black surface. Figure 3-21 and Figure 3-22 show SEM images of the surface of the rod. The images show corrosion products in the form of crystals following the grind lines from specimen preparation. The crystals tend to accumulate more sharply in some rows. The EDS analysis shows that the crystals are composed primarily of Cu and S elements (see Figure 3-22).
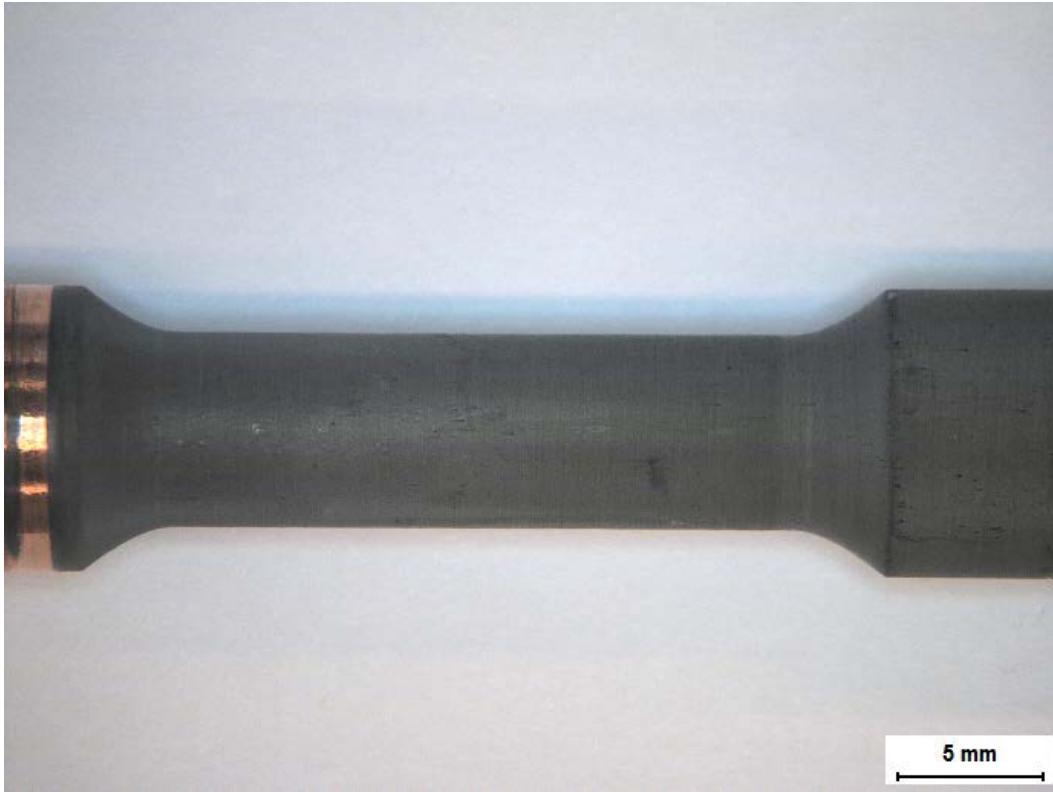
Figure 3-20. *LOM image of test Rod #6 (2021.6).*
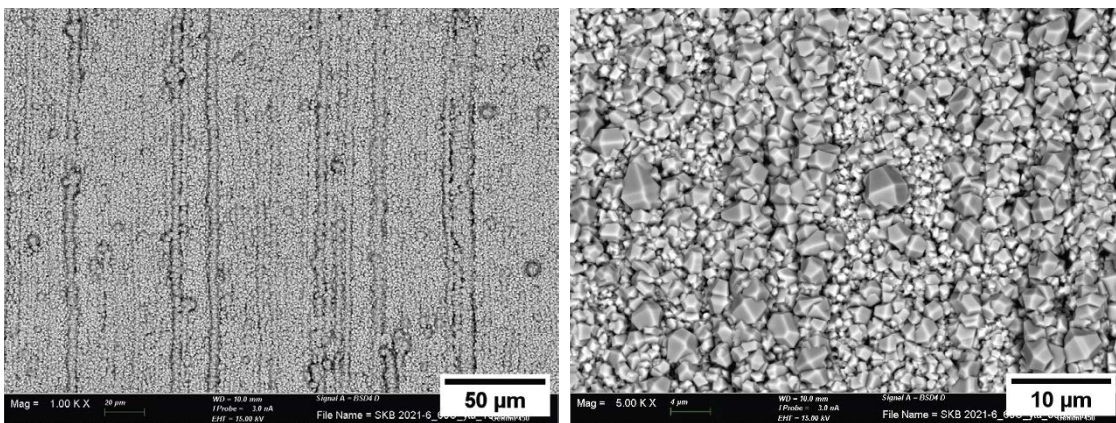
Figure 3-21. *SEM images of test Rod #6 (2021.6) (BSD mode, 15 kV). Left image shows grind lines from grinding and corrosion products following said lines, with some rows appearing more prominent than others. The right image shows a magnification of the corrosion products, which are of crystalline form.*
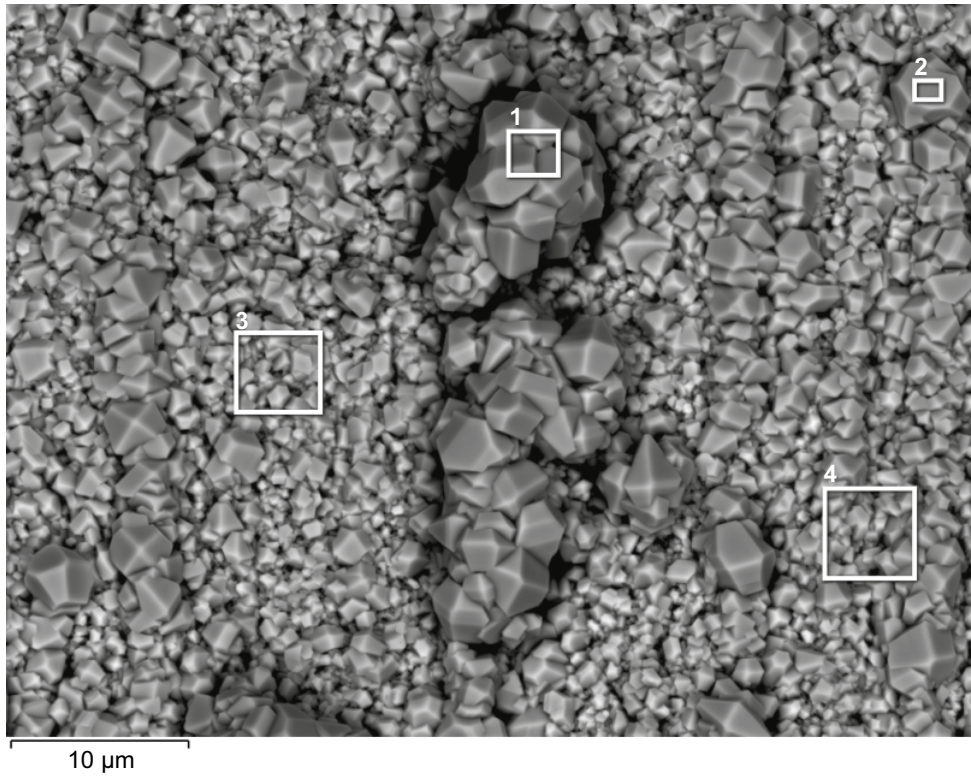
Spectrum label	O	Si	S	Cu	Total
1	2.38	0.22	28.61	68.79	100.00
2	1.85	0.27	28.80	69.07	100.00
3	2.71	0.22	29.17	67.89	100.00
4	2.57	0.27	29.39	67.76	100.00

***Figure 3-22.*** *SEM image and EDS analysis of the test Rod #6 (2021.6). The location of the areas shown in the image correspond to the spectrum labels in the table. The element analysis by EDS is shown in atomic percent. The atomic distribution is close to the expected for Cu_2S. The small amount of silicon is most likely traces from the polishing procedure, and the oxygen probably comes from atmospheric exposure.*

3.6 Metallographic examinations – Cross sections

As in the previous study, a number of SEM images of longitudinal cross sections after exposure were taken to assess feature morphology and estimate their length. Unexposed cross sections were investigated in an earlier study (Taxén et al. 2019).
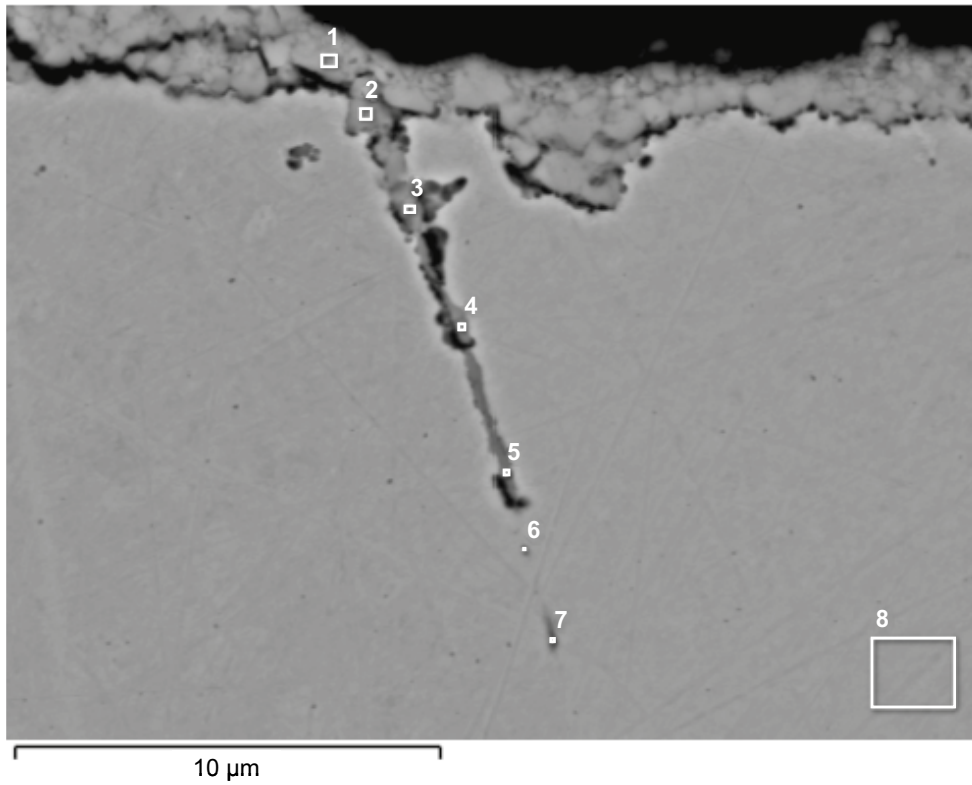
3.6.1 Rod #1 (2021.1), 60 °C, low strain rate

The following figures show selected images of features along the rod.
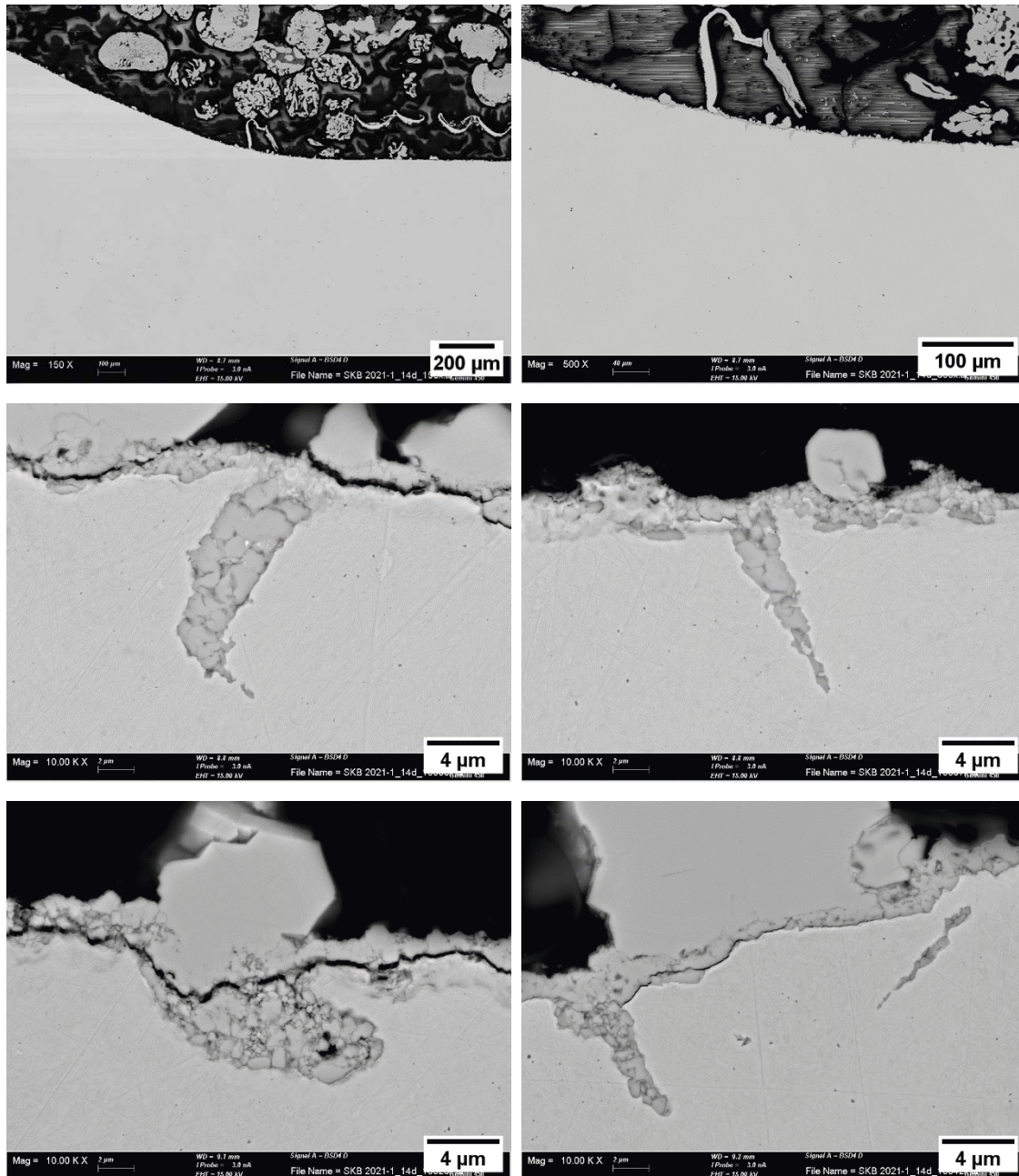
Figure 3-23. *Selected SEM images (SE, 15 kV) of features found in the cross section of Rod #1 (2021.1) at different magnifications.*

Spectrum label	O	Si	S	Cu	Total
1	2.68	0.68	28.85	67.78	100.00
2	3.22	0.43	24.45	71.90	100.00
3	4.35	0.47	19.64	75.54	100.00
4	2.01	0.42	17.46	80.11	100.00
5	1.55	0.33	16.35	81.76	100.00
6	1.00	0.30	2.75	95.94	100.00
7	7.87	0.26	0.0	91.87	100.00
8	0.73	0.28	0.0	99.00	100.00

Figure 3-24. *SEM image of a feature found in the cross section of Rod #1. The numbers refer to the elemental composition defined in the table, done by EDS and shown in atomic percent.*

3.6.2 Rod #2 (2021.2), 30 °C

The following figures show selected images of features along the rod.

Figure 3-25. *Selected SEM images of features found in the cross section of Rod #2 (2021.2) at different magnifications.*
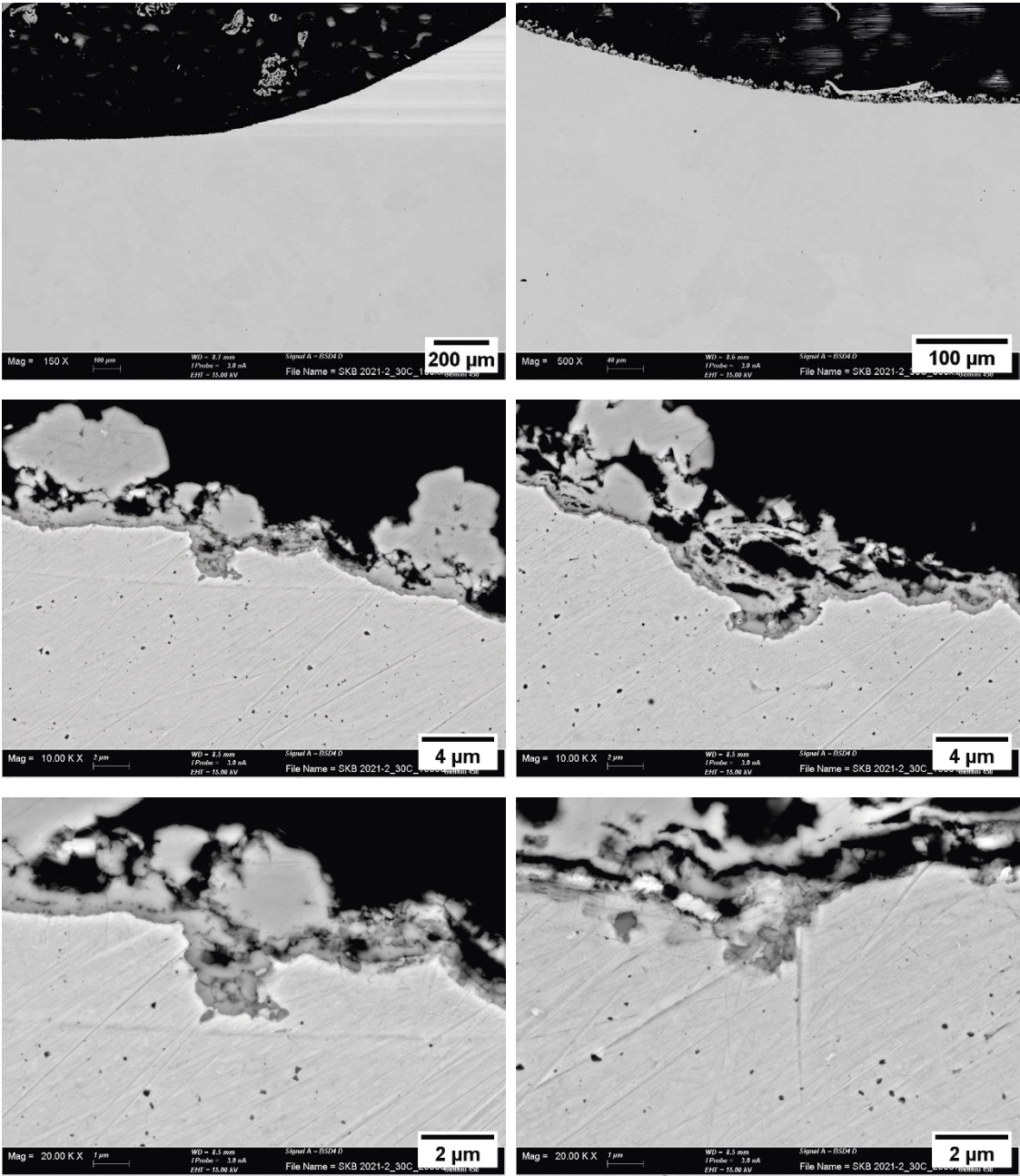
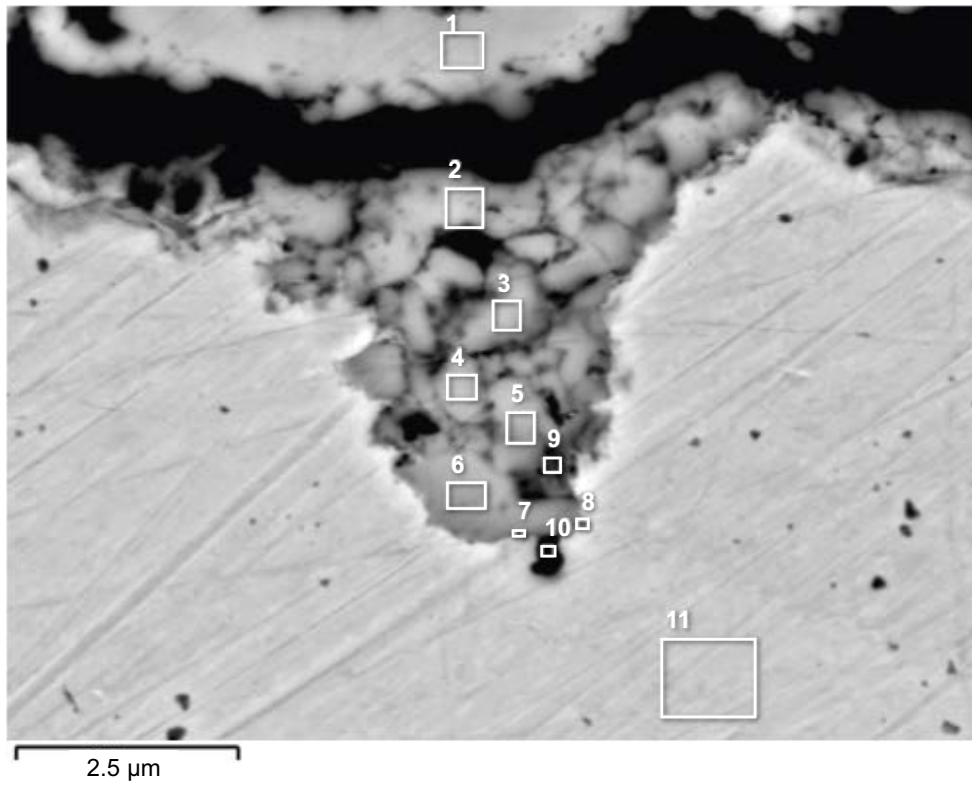| Spectrum label	O	Si	S	Cu	Total
1	1.36	0.26	29.26	69.12	100.00
2	2.15	0.30	28.51	69.04	100.00
3	2.36	0.39	28.68	68.57	100.00
4	2.37	0.29	28.70	68.65	100.00
5	2.22	0.42	27.93	69.43	100.00
6	1.56	0.24	26.60	71.60	100.00
7	1.98	0.39	23.29	74.34	100.00
8	1.98	0.22	4.62	93.18	100.00
9	3.66	0.54	22.87	72.93	100.00
10	2.87	0.45	13.53	83.15	100.00
11	1.07	0.32	0.0	98.61	100.00

Figure 3-26. *SEM image of a feature found in the cross section of Rod #2. The numbers refer to the elemental composition defined in the table, done by EDS and shown in atomic percent.*
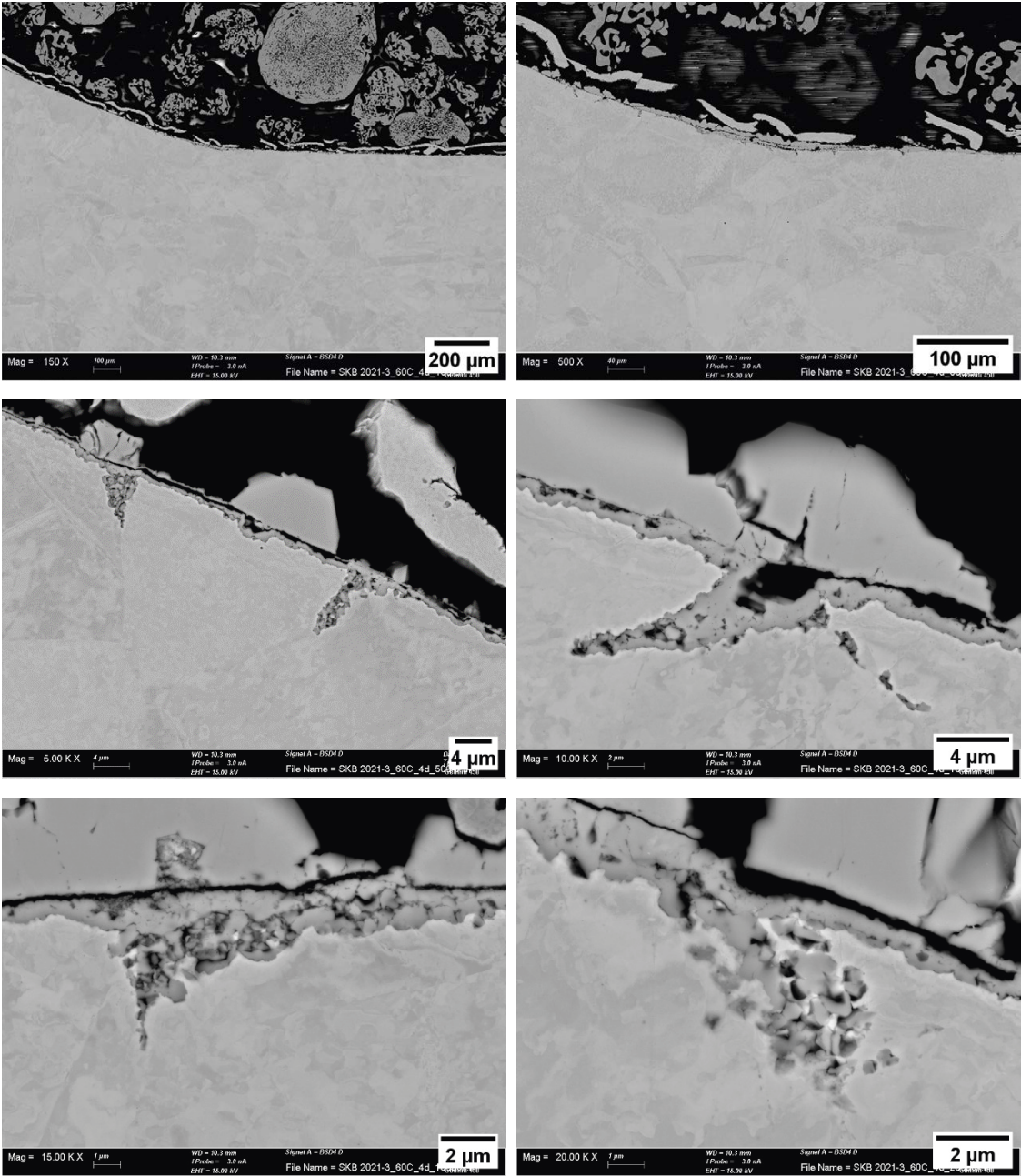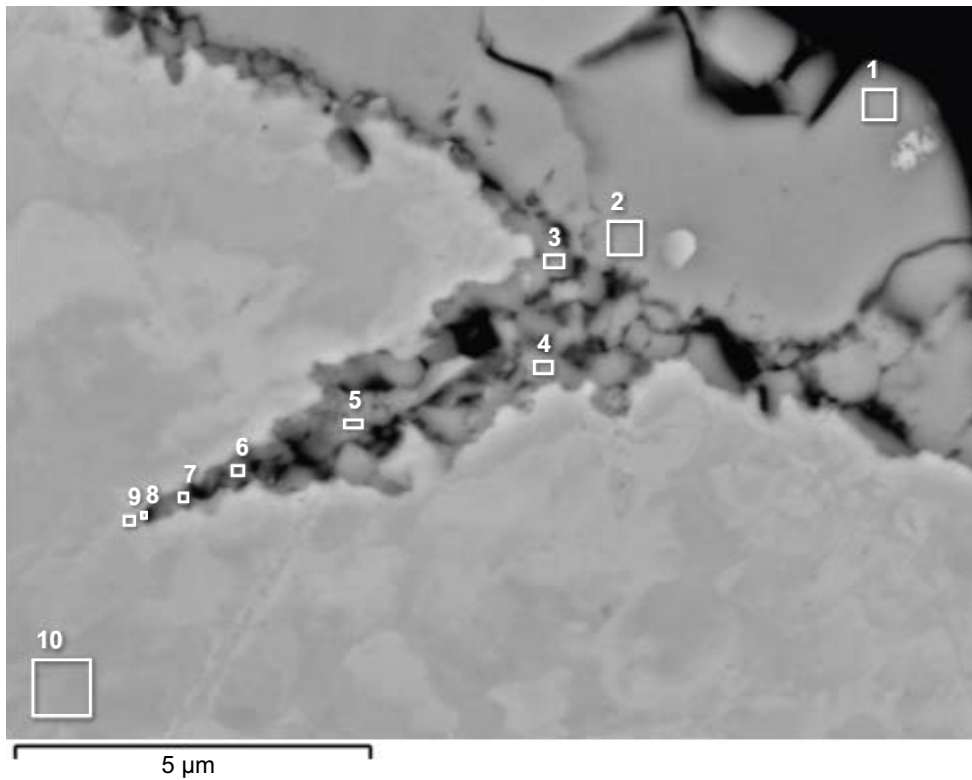
3.6.3 Rod #3 (2021.3), 60 °C, finely polished

Figure 3-27. *Selected SEM images of features found in the cross section of Rod #3 (2021.3) at different magnifications.*

Spectrum label	O	Si	S	Cu	Total
1	1.19	0.30	31.73	66.78	100.00
2	1.36	0.21	32.12	66.30	100.00
3	3.75	0.25	30.52	65.48	100.00
4	1.81	0.33	7.37	90.49	100.00
5	3.00	0.34	22.40	74.27	100.00
6	1.38	0.30	3.95	94.37	100.00
7	0.92	0.31	0.61	98.16	100.00
8	0.71	0.32	0.0	98.97	100.00
9	0.36	0.17	0.0	99.47	100.00
10	0.67	0.37	0.0	98.96	100.00

Figure 3-28. *SEM image of a feature found in the cross section of Rod #3. The numbers refer to the elemental composition defined in the table, done by EDS and shown in atomic percent.*

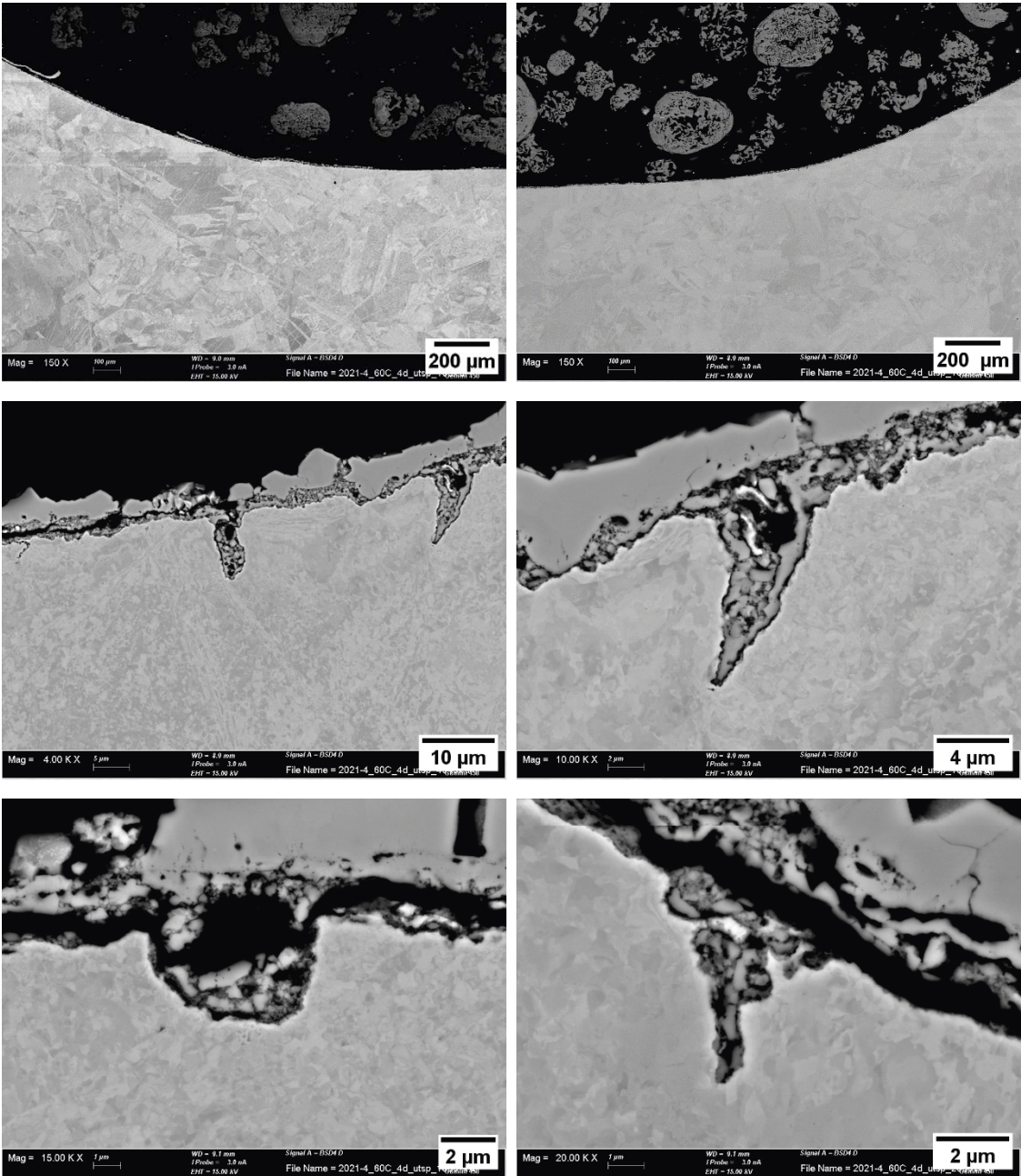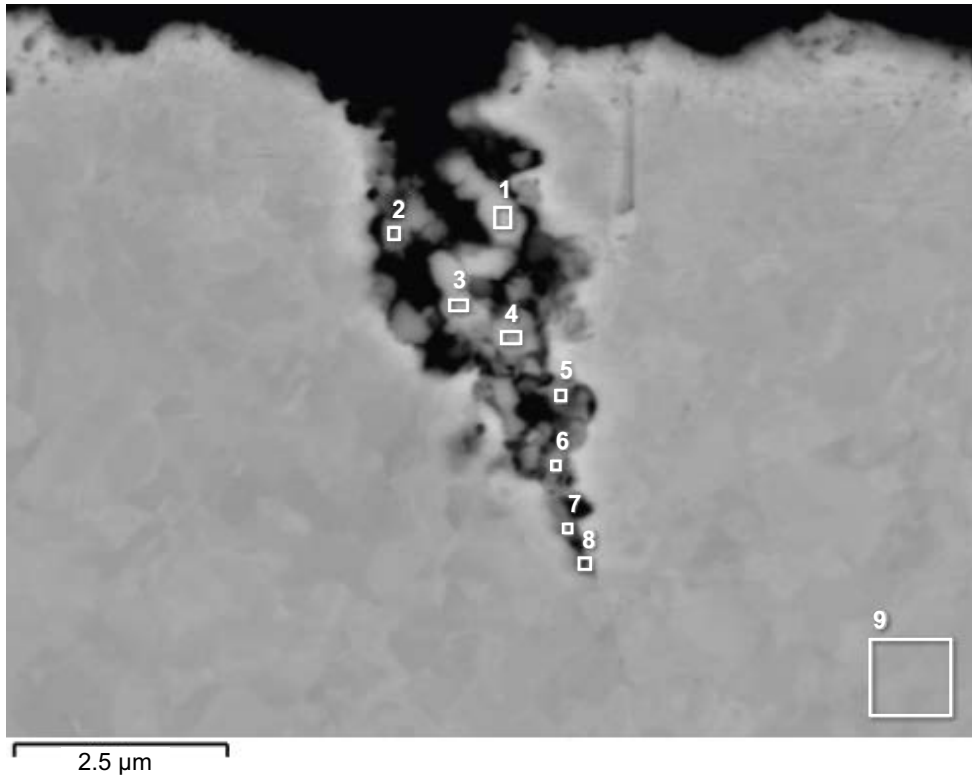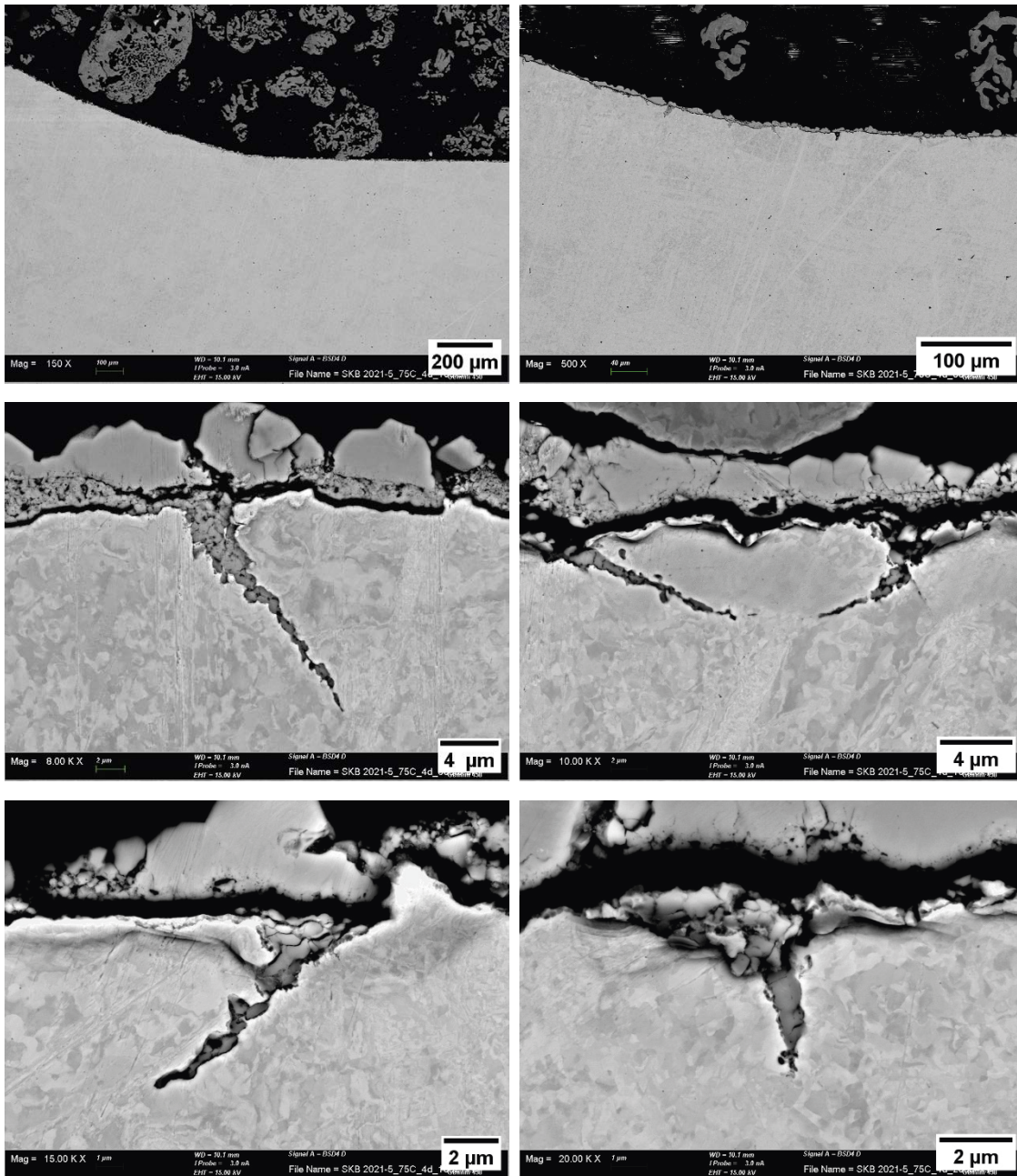### 3.6.4 Rod #4 (2021.4), 60 °C, 1 mM phosphate buffer + 1 mM chloride

Figure 3-29. *Selected SEM images of features found in the cross section of Rod #4 (2021.4) at different magnifications.*

Spectrum label	O	Si	S	Cu	Total
1	5.54	0.81	23.38	70.27	100.00
2	12.14	1.81	21.61	64.44	100.00
3	6.40	1.28	25.43	66.88	100.00
4	5.05	0.40	21.16	73.38	100.00
5	5.66	0.33	14.29	79.72	100.00
6	7.28	0.52	13.30	78.90	100.00
7	5.21	0.63	6.88	87.29	100.00
8	2.12	0.23	3.72	93.93	100.00
9	0.57	0.34	0.0	99.09	100.00

Figure 3-30. SEM image of a feature found in the cross section of Rod #4. The numbers refer to the elemental composition defined in the table, done by EDS and shown in atomic percent.

3.6.5 Rod #5 (2021.5), 75 °C

Figure 3-31. *Selected SEM images of features found in the cross section of Rod #5 (2021.5) at different magnifications.*

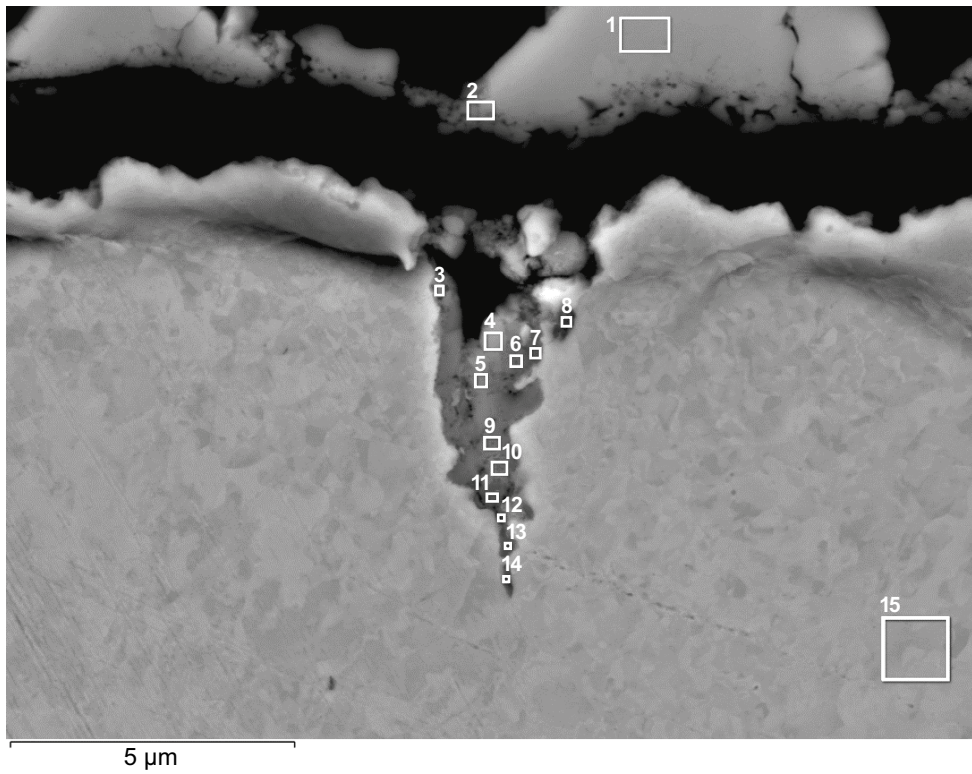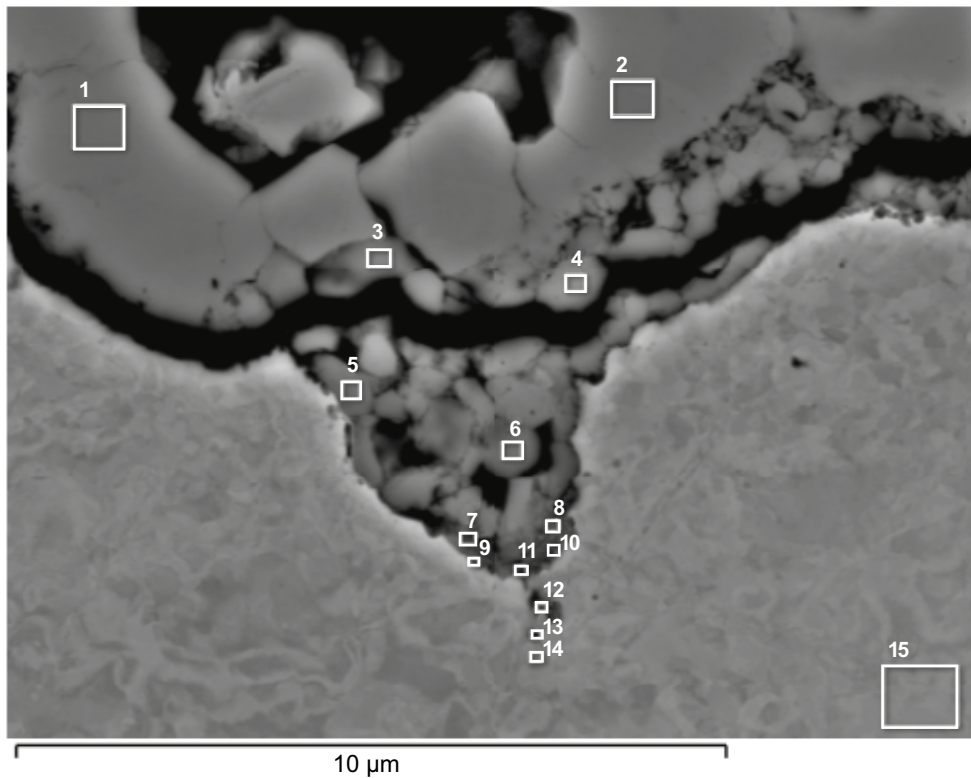| Spectrum label	O	Si	S	Ca	Cu	Total
1	2.41	0.48	29.91	0.0	67.20	100.00
2	9.12	2.37	27.14	0.10	61.27	100.00
3	8.25	0.91	12.15	0.11	78.58	100.00
4	6.72	0.67	24.68	0.09	67.85	100.00
5	5.48	0.37	23.98	0.0	70.17	100.00
6	7.36	0.44	19.17	0.0	73.03	100.00
7	6.66	0.34	12.31	0.0	80.70	100.00
8	4.65	0.32	8.64	0.0	86.39	100.00
9	4.08	0.23	23.14	0.0	72.55	100.00
10	6.95	0.25	20.58	0.0	72.22	100.00
11	5.43	0.32	15.29	0.0	78.96	100.00
12	9.55	0.39	5.23	0.0	84.83	100.00
13	5.88	0.42	4.51	0.0	89.19	100.00
14	4.07	0.30	1.19	0.0	94.43	100.00
15	0.81	0.29	0.0	0.0	98.90	100.00

Figure 3-32. *SEM image of a feature found in the cross section of Rod #5. The numbers refer to the elemental composition defined in the table, done by EDS and shown in atomic percent.*

3.6.6   Rod #6 (2021.6), 60 °C, borate buffer

Figure 3-33. *Selected SEM images of features found in the cross section of Rod #6 (2021.6) at different magnifications.*

Spectrum label	O	Si	S	Cu	Total
1	0.65	0.16	29.41	69.78	100.00
2	0.59	0.19	29.66	69.57	100.00
3	1.82	0.18	28.72	69.28	100.00
4	1.86	0.15	28.43	69.56	100.00
5	3.25	0.26	25.39	71.09	100.00
6	1.81	0.23	27.80	70.17	100.00
7	5.64	0.30	17.18	76.89	100.00
8	3.86	0.16	21.27	74.70	100.00
9	4.76	0.32	9.82	85.09	100.00
10	3.58	0.21	20.69	75.51	100.00
11	5.94	0.17	17.46	76.43	100.00
12	4.77	0.18	11.90	83.14	100.00
13	1.81	0.22	5.51	92.45	100.00
14	0.75	0.26	0.22	98.77	100.00
15	0.51	0.19	0.0	99.30	100.00

Figure 3-34. *SEM image of a feature found in the cross section of Rod #6. The numbers refer to the elemental composition defined in the table, done by EDS and shown in atomic percent.*

3.7 TEM results

Two specimens (Rod #3 and Rod #4) were selected to be analysed using FIB/TEM. A feature was chosen from each specimen and a lamella was manufactured in that position.

The main result of the TEM study was the identification of phases, most likely Cu_2S and Cu_2O, however not entirely conclusive due to the difficulties in lamellae handling and a potential contamination during sample preparation. The copper oxide layer was found at the interface between the Cu_2S layer and the base metal.

A summary of the TEM analysis results is presented in Appendix A.

3.8 Feature density

Feature density was determined using the SEM-images of longitudinal cross sections, which in the previous study were deemed to be a sensitive method for detecting cracks or crack-like features. The number of features was recorded for each millimetre in the longitudinal direction of the rod and then plotted as number of features (cracks) per mm. All plots have the same scale.
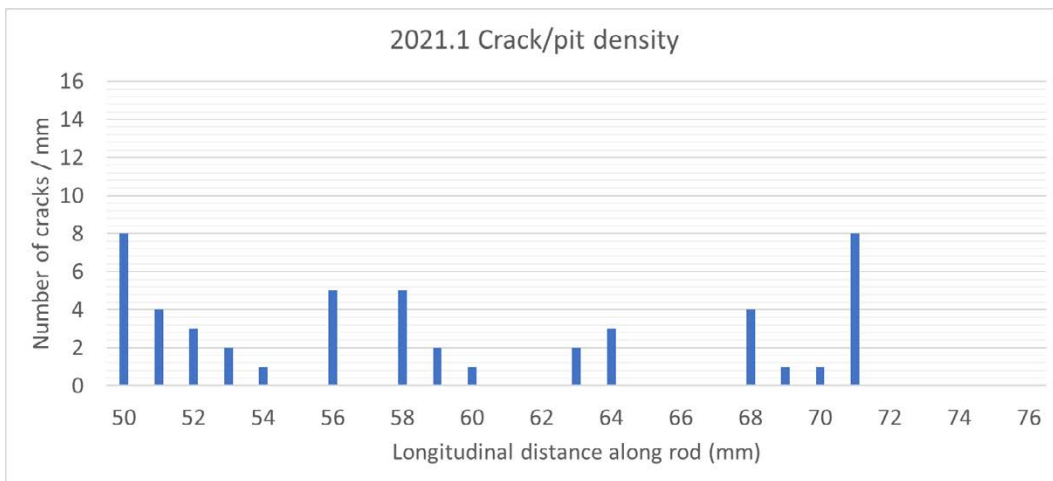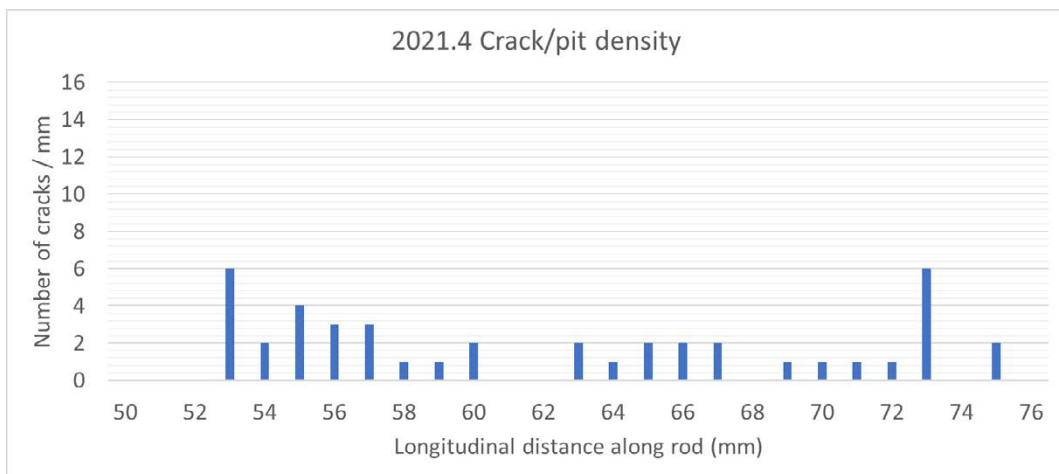

Figure 3-35. Features per millimetre in the longitudinal distance along the Rod #1 (2021.1). The total number of recorded features is 50.
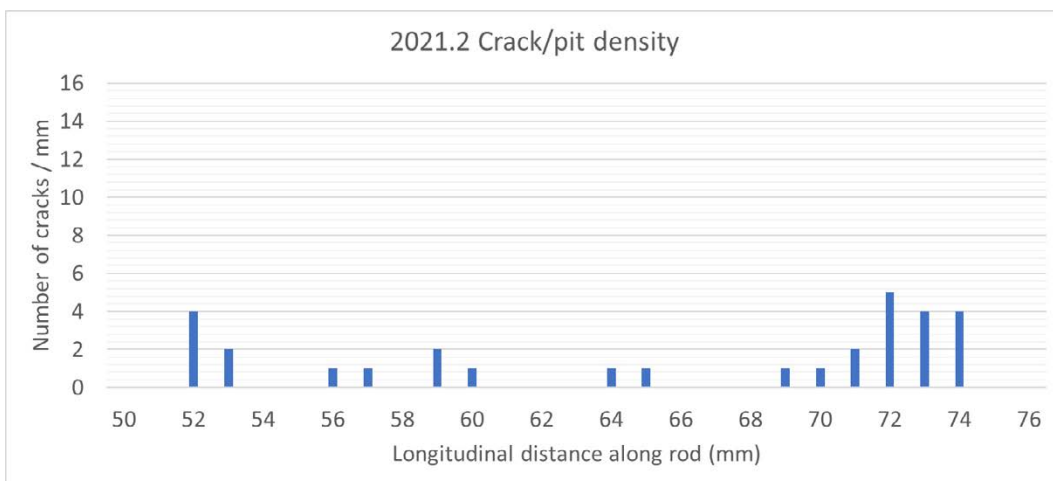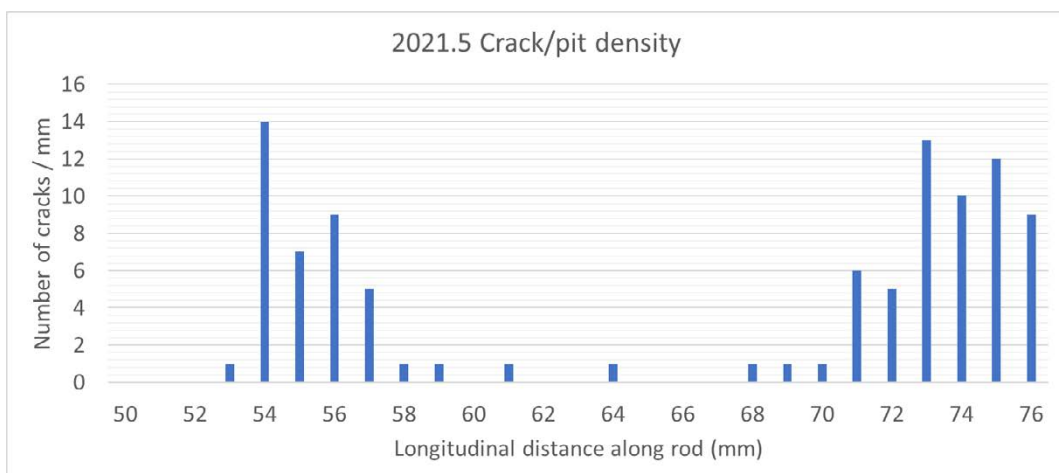

Figure 3-36. Features per millimetre in the longitudinal distance along the Rod #2 (2021.2). The total number of recorded features is 30.
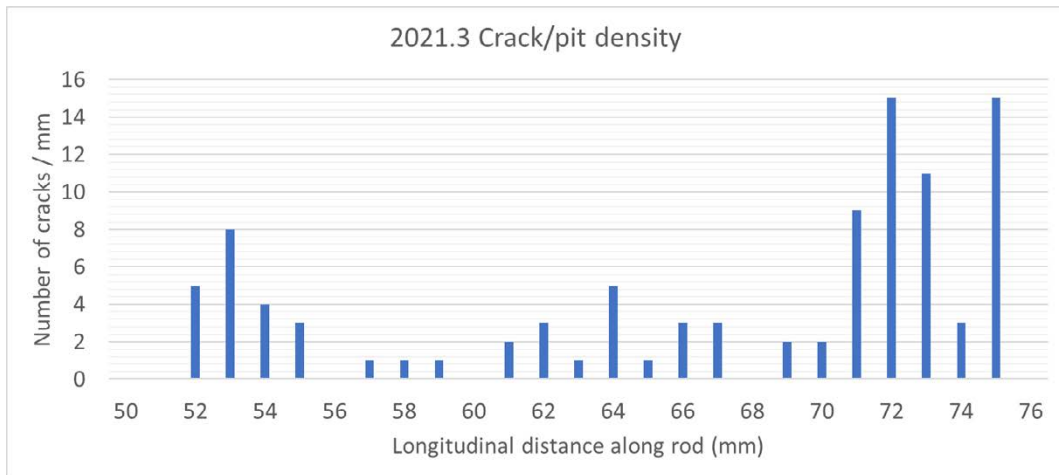
***Figure 3-37.** Features per millimetre in the longitudinal distance along the Rod # 3 (2021.3). The total number of recorded features is 98.*

***Figure 3-38.** Features per millimetre in the longitudinal distance along the Rod #4 (2021.4). The total number of recorded features is 43.*
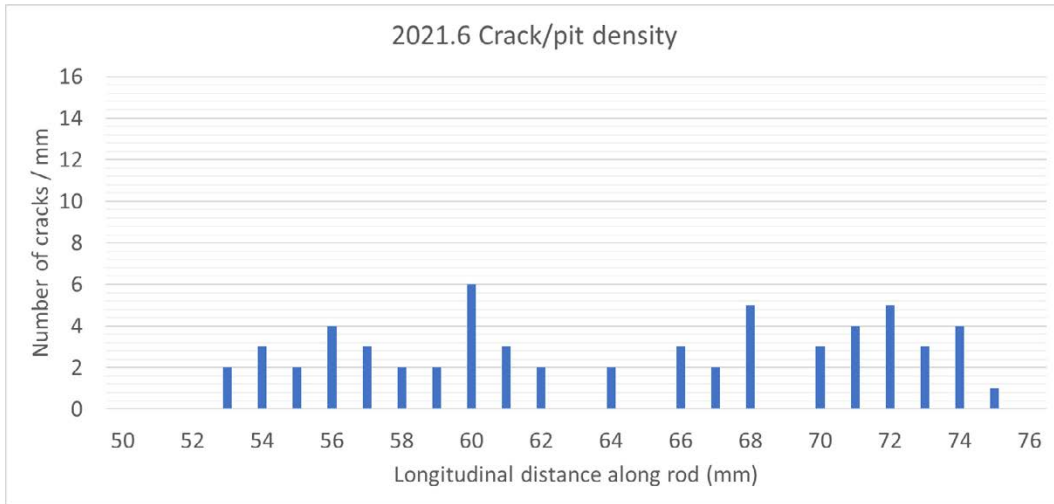

***Figure 3-39.** Features per millimetre in the longitudinal distance along the Rod #5 (2021.5). The total number of recorded features is 98.*

Figure 3-40. *Features per millimetre in the longitudinal distance along the Rod #6 (2021.6). The total number of recorded features is 61.*

3.9 Feature length

The feature length was measured in selected SEM images for each specimen, from a representative selection. The shape and orientation of the features was taken into account by measuring the length instead of the depth. This measurement was done starting from a subjective baseline, assumed to correspond to the surface of the metal, following the feature's shape up to the tip. A histogram is presented for each run (features' frequency versus feature length). The measurements were done using SEM images imported to the software ImageJ. All plots have the same scale.
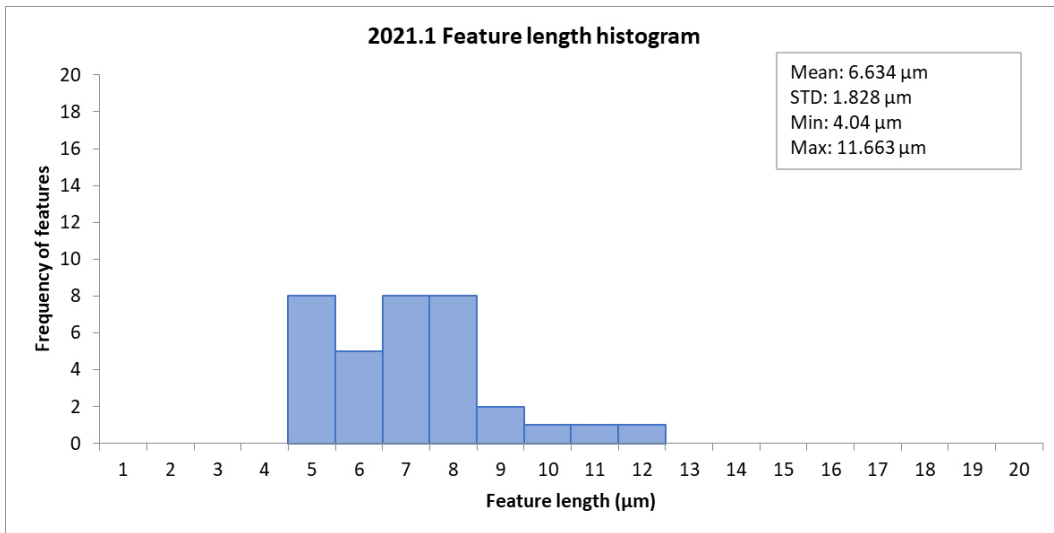
Figure 3-41. *Feature length in μm versus their frequency in Rod #1 (2021.1).*
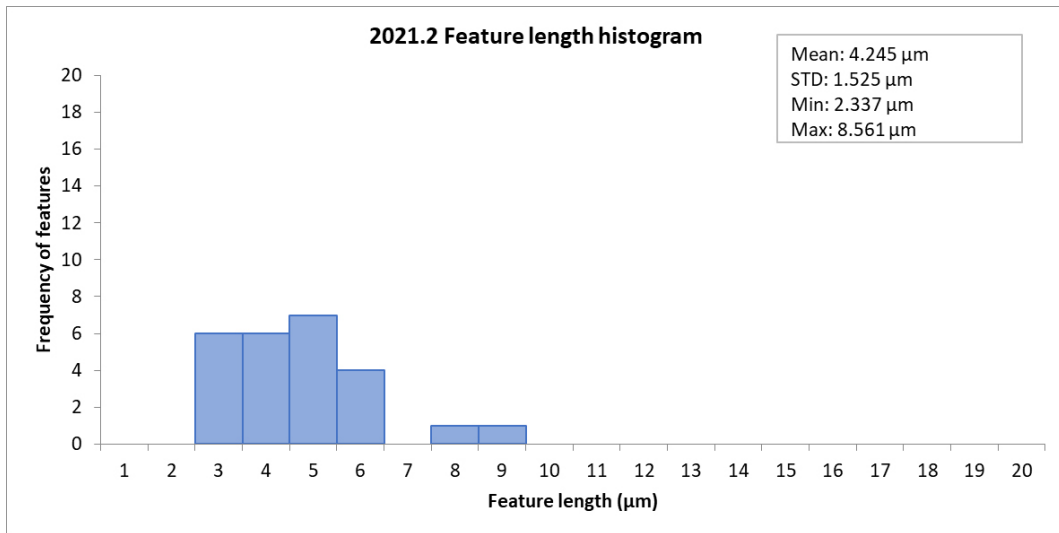
Figure 3-42. *Feature length in µm versus their frequency in Rod #2 (2021.2).*
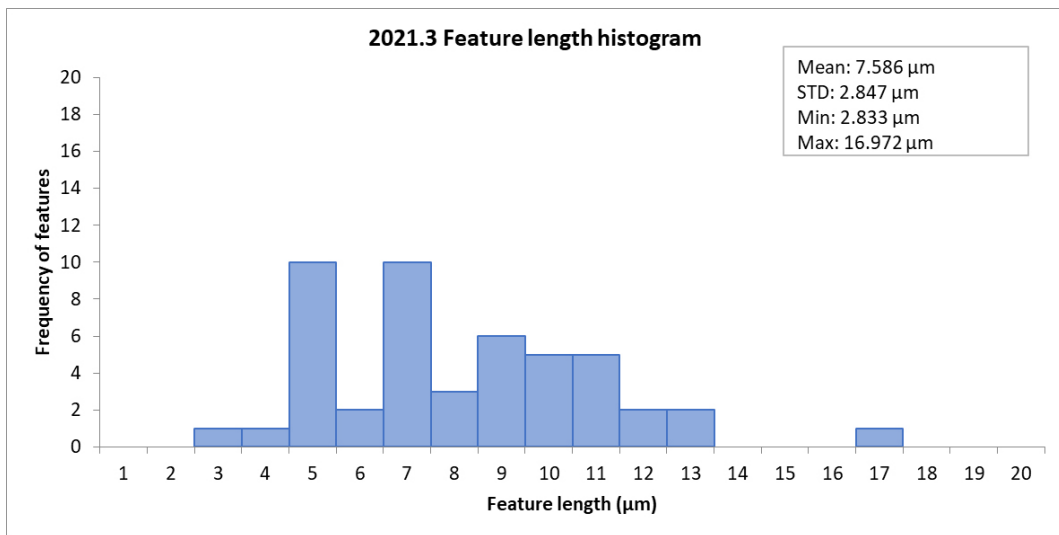
Figure 3-43. *Feature length in µm versus their frequency in Rod #3 (2021.3).*

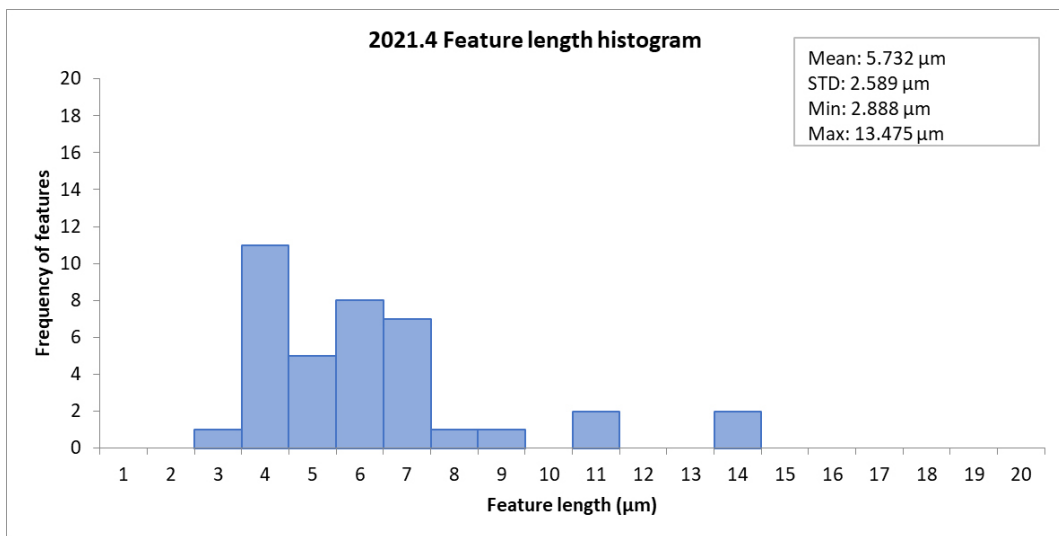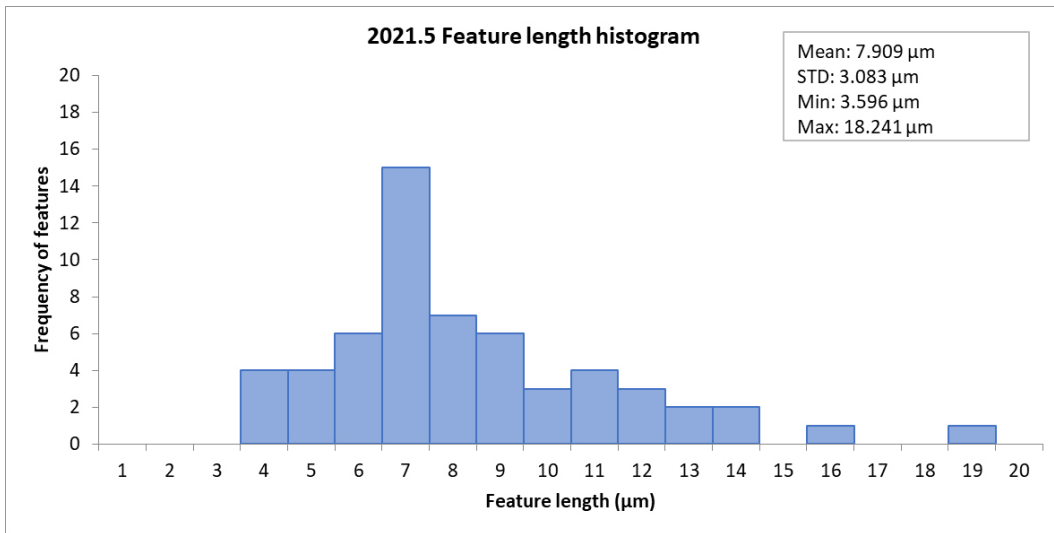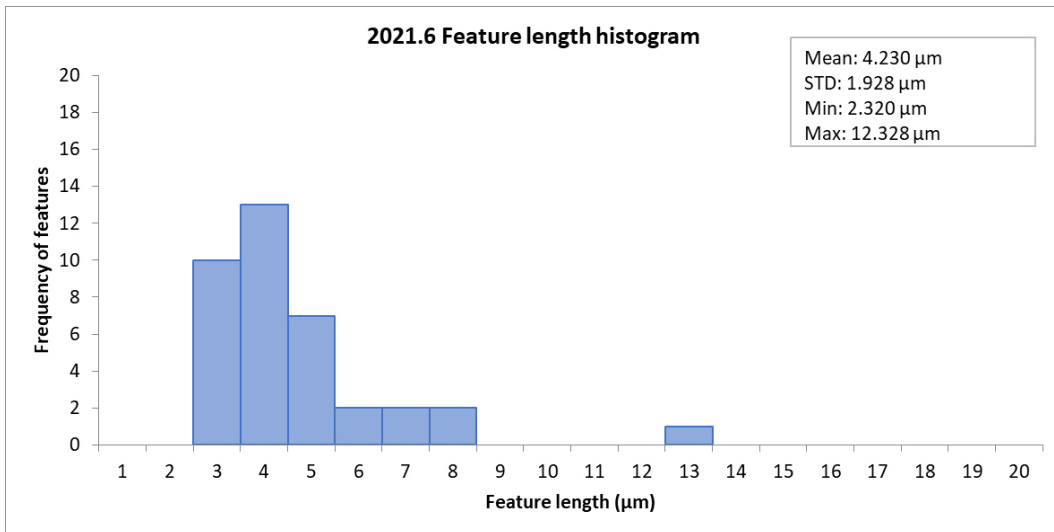***Figure 3-44.*** *Feature length in µm versus their frequency in Rod #4 (2021.4).*

Figure 3-45. *Feature length in μm versus their frequency in Rod #5 (2021.5).*

Figure 3-46. *Feature length in μm versus their frequency in Rod #6 (2021.6).*

4 Discussion

4.1 Comments on the experimental results

Stress-strain curves in Figure 3-1 show no signs of cracking. At these relatively low levels of stress and strain, a cracking event could manifest as a drop of the stress required to maintain the stress and strain rate. The corrosion potential and measured Pt-potentials are consistent between the runs. Only Rods #2 (30 °C) and #6 (solution C) gave slightly higher Pt-potentials (Figure 3-2).

The sulfide concentrations measured at the sampling valve show consistent values (Figure 3-3). The small dip after about 166 hours in Rod #1 corresponds to a renewal of the stock solutions.

The pH-values of the test solutions in Figure 3-4 show consistent values of about 7.5. Only the Rod #6, in solution C, resulted in higher value of about pH 8.2. As observed in Table 2-1 the buffer capacity of solution C is relatively low under neutral conditions.

Appearance of the outer surface of the test rods after testing

The exposed sections of the test rods generally had a black color. Some flaking can be observed, for example in Figures 3-14 and 3-15 from Rod #4. SEM-images of the outer surfaces of the test rods show a mixture of small and larger crystals. The largest crystals were found on Rod #1 (Figure 3-6). The smaller crystals seem to follow an underlying pattern of scratches from the grinding and polishing of the test rods. At some locations the pattern seems more complex which may be related to previous flaking of corrosion products during the test (Figure 3-12 and 3-15).

Location and number of features in longitudinal cross sections

The diagrams in Figures 3-35 to 3-40 show that the features are predominantly located towards the ends of the gauge section. This was also observed in our previous study (Taxén et al. 2019). In the present study, this is most clear in Figures 3-37 and 3-39. No credible chemical explanation for the concentration of attacks towards the ends has been found. The reason may be mechanical and related to a higher surface stress at locations influenced by the proximity to the transition to a larger diameter.

The highest density of the features is found in Figures 3-37 and 3-39 corresponding to Rod #3 with the fine polished test rod at 60 °C and Rod #5 with at 75 °C, respectively. The fewest and shallowest (< 10 µm in length) features are seen in Figure 3-36 from Rod #2 at 30 °C.

It is also noted that the runs in solutions with low conductivity and low buffer capacity, resulted in relatively few and shallow features (approximately < 13 µm in length). Rod #4 in solution B in Table 2-1 (Figure 3-38) and Rod #6 in solution C in Table 2-1 (Figure 3-40) both resulted in fewer features than Rod #3 in solution A in Table 2-1, at the same temperature. The fact that Rod #3 used a finer polished rod is not likely to have increased the number of features and the effect is more likely due to the composition of the test solution.

Increasing temperature 30 °C, 60 °C, 75 °C gives higher number of features which are more crack-like than pit-like at the higher temperatures.

Rod #6 in borate solution (solution C) resulted in some crack-like features, indicating that stress corrosion is not limited to phosphate solutions. The relatively low number of features from Rod #6 may be explained by relatively low buffer capacity of solution C, at neutral pH which allowed the pH to increase (Figure 3-4). As discussed in TR-19-13, the driving potential for corrosion decreases with increasing pH. A lower force could manifest as a lower number of localized corrosion attacks.

The appearance of the corrosion products in the crack-like features

SEM-images of longitudinal cross sections of the test rod from Rod #1 show that the crack-like features are filled with solids. In Rods #2 to #6 the features seem more open and to have contained a much larger aqueous fraction (filled with solution). The main difference in test conditions is that Rod #1 used a strain rate of 1×10^{-7} s^{-1} and lasted 14 days whereas in Rods #2 to #6 the strain rate was 5×10^{-7} s^{-1} and the tests were interrupted after 4 days.

TEM results

The objective of the TEM study was to examine any differences in the crystalline corrosion products at different positions along the features. The results, however, were inconclusive due to difficulties during the lamellae extraction and overall analysis interpretation; during FIB the corrosion products were milled away at a higher rate by the ion beam than the base metal, leading to excessive material loss. There were not enough corrosion products to identify them accurately using electron diffraction. Furthermore, two areas of each feature were to be examined in the same lamella, which proved to be deleterious for the quality of the sample. The recommendation for future TEM work is to prepare the lamellae along the crack propagation direction, in order to achieve higher quality and acquire more information about the crack growth.

The main result of the work was the identification of a thin copper oxide layer in the interface between the Cu$_2$S layer and the base metal, and this is believed to originate after the SSRT exposure, during specimen handling. Copper oxides are not stable under the conditions of the SSRT exposure.

The TEM results and further discussions are presented in Appendix A.

4.2 Summary of observations from literature 2018–2022

Several papers dealing with copper corrosion in sulfidic environment were published in a special issue of Material and Corrosion (Vol 72, Issue 1-2). A more extensive survey of relevant literature was made previously (Taxén et al. 2018) and complemented here with more recent publications.

Senior et al. (2021) studied the effect of sulfide on copper by detection of the hydrogen formed. They found that more hydrogen than expected was formed than corresponds to a monolayer of copper sulfide. After a first rapid corrosion, subsequent additions of sulfide did not result in further oxidation. The authors conclude that the slightly corroded surface is in a more stable state due to oxidation of non-terrace atoms and surface rearrangements (during the first rapid corrosion).

Fujimoto et al. (2021) studied Stress Corrosion Cracking of copper, by SSRT, in swollen bentonite with pure water or with NH$_3$. They found a tarnish crack type SCC. The oxide layer ruptures under strain with or without NH$_3$. The swollen bentonite was prepared in laboratory atmosphere and used without any deaeration.

Forsström et al. (2021) studied SKB-copper for SCC in solutions with 1 mM or 0.01 mM sulfide at 90 °C using SSRT with tapered test rods. In parallel experiments friction stir welds were exposed to solutions with 0.01 or 1.0 mM sulfide. The authors conclude that SCC occurs at a sulfide concentration of 1 mM at 90 °C. Friction stir welds were found to contain oxygen particles that were rapidly converted to copper sulfide. Increased hydrogen content in the copper was observed in both types of experiments. This paper seems to be a condensed version of the following report by Becker et al. (2020).

Becker et al. (2020) studied "*Sulfide-induced stress corrosion cracking and hydrogen absorption in copper exposed to sulfide and chloride containing deoxygenated water at 90 °C*". They used tapered test rods and the SSRT experiments in 1 mM or 0.01 mM sulfide lasted four weeks. Optical study revealed at least three types of layers where a new layer forms where previous corrosion products have detached (1 mM sulfide). They found defects in the exposed rods beneath the corrosion products. EBSD (Electron backscatter diffraction) confirmed that these defects were inter-crystalline. No such defects were found after test in 0.01 mM sulfide. Friction stir welds were exposed to sulfide solutions in the same study. Increased hydrogen content was found in specimens exposed to 1 mM sulfide and the increase was higher for the loaded specimen than for the unloaded.

Guo et al. (2021) studied the properties of copper sulfide films grown anodically or naturally. For solutions with between 5×10^{-5} and 5×10^{-4} M sulfide at pH 8 (borate buffer) they found that low concentrations yielded one single thin layer and that an outer crystalline layer deposited at higher concentrations. It was concluded that the layers had barrier effects but were not passivating.

Guo et al. (2019) studied the susceptibility of copper to pitting corrosion in borate-buffered aqueous solutions containing chloride and sulfide. The authors conclude that if pitting is to occur on Cu, it will require oxide not sulfide film growth. This seems to be based on the finding that sulfide films are not passive. That the Cu_2S film remained porous and non-passive was confirmed by the revival of partially transport controlled Cu_2S growth once any oxide films formed at more positive potentials had been removed. No evidence for pitting was observed at any potential and would only be expected at potentials sufficiently positive for oxide formation.

Guo et al. (2020) report on the anodic formation of sulfide and oxide films on copper in borate-buffered aqueous chloride solutions containing sulfide. By electrochemical stimulation of the corrosion they were able to study the formation of aqueous chloride complexes with copper as well as oxide and sulfide films. A main purpose was to characterize corrosion films and to investigate the tendency for passivation and pitting. They characterized a film of Cu_2S with an inner thin layer and an outer layer of growing crystals. The inner layer was not passivating and became porous.

Zhang et al. (2021) exposed copper in 1 mM sulfide for 53 days at 22 °C. Synchrotron high-energy XRD measurements was applied to exposed and unexposed samples. An increased bond length or lattice expansion was detected in the exposed sample relative to the unexposed. This is taken as evidence for the absorption of hydrogen into the metal, apparently to a depth of about 400 µm. The authors support the findings with DFT (Density Functional Theory)-calculations but no quantification or independent verification of the presence of hydrogen is reported. Comments and a reply to comment on this paper have also been published.

Halldin Stenlid et al. (2021) applied DFT to study the properties of interfaces between copper and copper sulfide/oxide films. The authors discuss energetically favourable boundaries between copper metal and its corrosion products to explain differences in adherence. It was found that Cu_2S forms only on some crystallographic copper facets which was suggested as an explanation for the observed poor adherence of Cu_2S on copper. The use of bulk properties of corrosion products to predict properties of thin films is discouraged.

5　Conclusions

Slow strain rate tests were performed at 30 °C, 60 °C and 75 °C at pH about 7.2 in solutions of 1.0 mM sulfide. After the tests and examinations reported here we suggest that the following conclusions can be drawn from the results.

- The results in the present study agree well with our previous findings (Taxén et al. 2019).

- Stress/strain curves do not reveal any sign of stress corrosion cracking.

- A number of corrosion attacks can be seen on longitudinal cross sections of the exposed rods. Some features appear crack-like and others pit-like. All crack-like features seem to be intergranular.

- The maximum length of a corrosion attack found was about 20 µm (Rod #5 at 75 °C). The depth measured from the surface was lower because of the angle of the crack-like feature.

- The increase in temperature from 60 °C to 75 °C generally did not result in deeper or a higher number of corrosion attacks but the features seem more crack-like after test at 75 °C than at 60 °C.

- The degree of polishing of the test rods does not seem to have any effect on the number and depth of the corrosion attacks. A fine polished rod does not give fewer or less shallow corrosion attacks.

- The test performed at 30 °C resulted in a low number of corrosion attacks that were relatively shallow (< 10 µm).

- The test performed in a pH buffer of borate instead of phosphate also resulted in shallow corrosion attacks (< 13 µm). Possibly because the low buffer capacity of borate at neutral pH allowed the pH to increase to a level where the solution was less corrosive.

- The hypothesis that the cause of the appearance of crack-features is intergranular corrosion aggravated by strain (Taxén et al. 2019) is supported by the results presented here.

- There was an attempt to perform phase identification on corrosion products using FIB/TEM (two features in Rod #3 and Rod #4). The results from the phase identification using diffraction data were inconclusive. The TEM study however confirms the presence of trace amounts of oxygen inside the features, as suggested by the SEM/EDS examination. The evidence from the STEM images does not contradict the explanation that the copper-oxygen compounds were formed after the exposure took place.

References

SKB's (Svensk Kärnbränslehantering AB) publications can be found at www.skb.se/publications.

Becker R, Forsström A, Yagodzinskyy Y, Hänninen H, Heikkilä M, 2020. Sulphide-induced stress corrosion cracking and hydrogen absorption in copper exposed to sulphide and chloride containing deoxygenated water at 90 °C. SSM report 2020:1, Swedish Radiation Safety Authority.

Birks N, Meier G, Pettit, F, 2006. Introduction to high temperature oxidation of metals. New York, NY: Cambridge University Press.

Forsström A, Becker R, Hänninen H, Yagodzinskyy Y, Heikkilä M, 2021. Sulphide-induced stress corrosion cracking and hydrogen absorption in copper exposed to sulphide and chloride containing deoxygenated water at 90 °C. Materials and Corrosion, Volume 72, 317–332.

Fujimoto S, Tsuchiya H, Ogawa S, Lida Y, Taniguchi N, 2021. Stress Corrosion Cracking of copper, by SSRT, in swollen bentonite simulating nuclear waste disposal environment. Materials and Corrosion, Volume 72, 333–338.

Guo M, Chen J, Lilja C, Dehnavi V, Behazin M, Noël JJ, Shoesmith D W, 2020. The anodic formation of sulfide and oxide films on copper in borate-buffered aqueous chloride solutions containing sulfide. Electrochimica Acta, 362(137087).

Guo M, Chen J, Martino T, Biesinger M, Noël J J, Shoesmith D W, 2019. The susceptibility of copper to pitting corrosion in borate-buffered aqueous solutions containing chloride and sulfide. Journal of The Electrochemical Society, 166(15), pp. C550–C558.

Guo M, Chen J, Martino T, Lilja C, Johansson J A, Behazin M, Binns W J, Keech P G, Noël J J, Shoesmith D W, 2021. The nature of the copper sulfide film grown on copper in aqueous sulfide and chloride solution. Materials and Corrosion, Volume 72, 300–307.

Halldin Stenlid J, Campos dos Santos E, Johansson A, Pettersson L G M, 2021. Properties of interfaces between copper and copper sulphide/oxide films. Corrosion Science, 183(Article 109313).

Lide D R, 2002–2003. CRC Handbook of Chemistry and Physics, 83rd Edition. Boca Raton, FL: CRC Press.

Schneider C A, Rasband W S, Eliceiri K W, 2012. NIH Image to ImageJ: 25 years of image analysis. Nature Methods, Issue 9, 671–675.

Senior N, Martino T, Binns J, Keech P, 2021. The anoxic corrosion behaviour of copper in the presence of chloride and sulphide. Materials and Corrosion, Volume 72, 282–292.

Stumm W, Morgan J J, 1981. Aquatic Chemistry: An Introduction Emphasizing Chemical Equilibria in Natural Waters. New York, NY: John Wiley & Sons Ltd.

Taxén C, Flyg J,Bergqvist H, 2018. Stress corrosion testing of copper in sulfide solutions. SKB TR-17-16, Svensk Kärnbränslehantering AB.

Taxén C, Flyg J, Bergqvist H, 2019. Stress corrosion testing of copper in near neutral sulfide solutions. SKB TR-19-13, Svensk Kärnbränslehantering AB.

Zhang F, Ornek C, Liu M, Müller T, Lienert U, Ratia-Hanby V, Carpén L, Isotahdon E, Pan J, 2021. Corrosion-induced microstructure degradation of copper in sulfide-containing simulated anoxic groundwater studied by synchrotron high-energy X-ray diffraction and ab-initio density functional theory calculation. Corrosion Science, 184(109390).

TEM Examination

A1   Experimental

Electron transparent lamellae were produced using focused ion beam (FIB) in situ lift-out. Lamellae were taken from 2 different exposures, at one position for each. The areas of interest were chosen in a way that both the crack tip and the surface interface would be present in the same lamella. A Zeiss Crossbeam FIB was used. The surface was protected by deposition of a Pt/C metallo-organic precursor, first using the electron beam at 3 keV and then Ga ions at 30 keV. The lamellae were cut out and then lifted out using a micromanipulator and mounted on a titanium grid. Then they were thinned down using Ga ions, starting with 30 keV energy and subsequently lowering the energy and current, ending with 2 keV to ensure a minimum of beam damage.

The lamellae were investigated in a JEOL 2100F (S)TEM (Scanning Transmission Electron Microscopy) at 200 keV. EDS was acquired using a windowless X-maxN detector from Oxford Instruments.

Some TEM analysis of samples tested by SSRT were made. The purpose was to obtain more detailed information about the chemical phases in and around the cracks.

A2   Results

The results of the TEM investigation are shown below. Some results were omitted due to suspected contamination during the lamella preparation process or handling. Fast Fourier Transforms (FFTs) meant to identify local crystal structure were omitted due to inconclusive phase identification.

A2.1   Rod #3

The lamella obtained from Rod #3 was lifted in the positions shown in Figures A-1 to A-5.
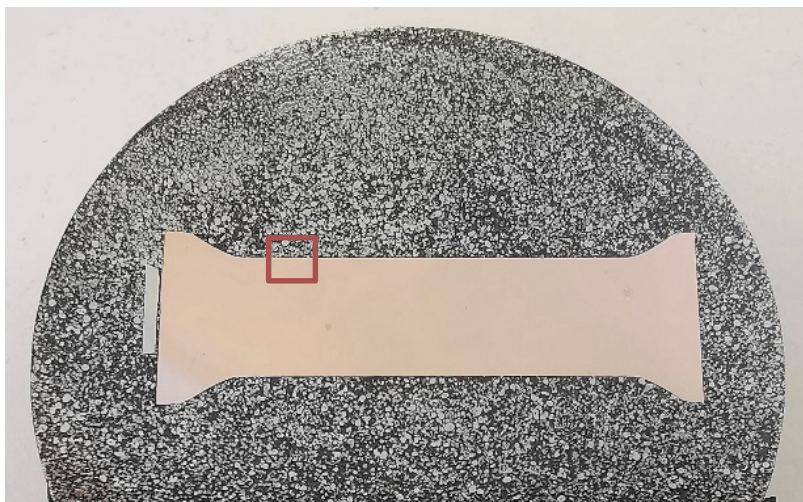
Figure A-1. *Longitudinal cross section of a copper rod mounted in bakelite. The red square shows the approximate site where the chosen feature for TEM analysis is located.*
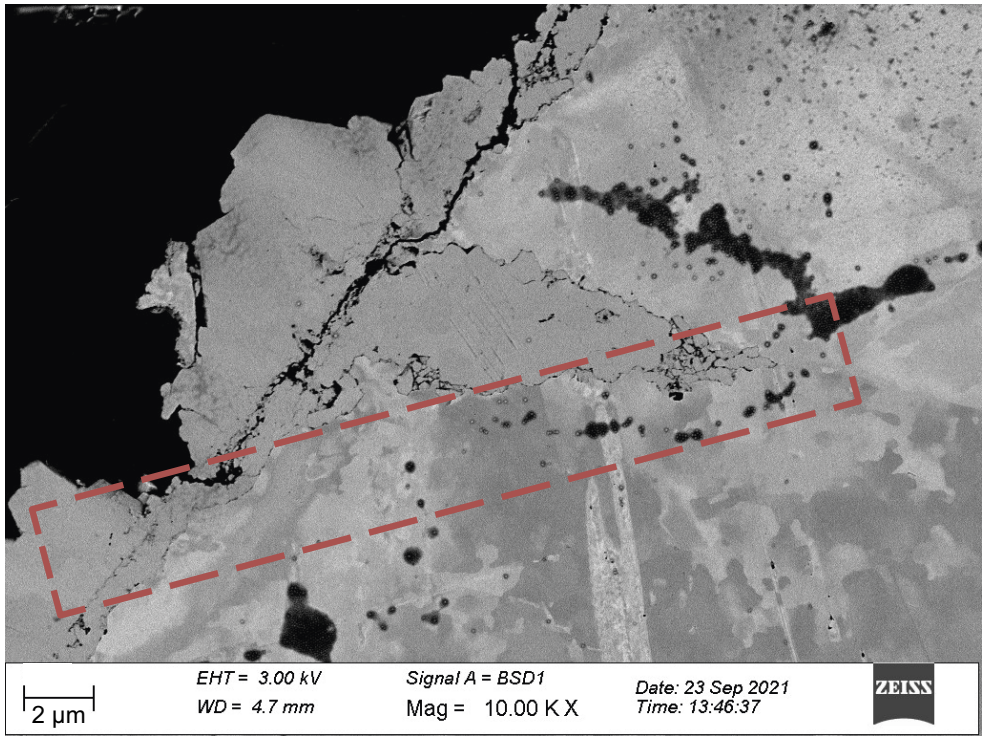
Figure A-2. *SEM image of the selected location for the FIB lamella in the cross section of Rod #3 (red dashed lines represent the approximate site where the lamella was lifted).*
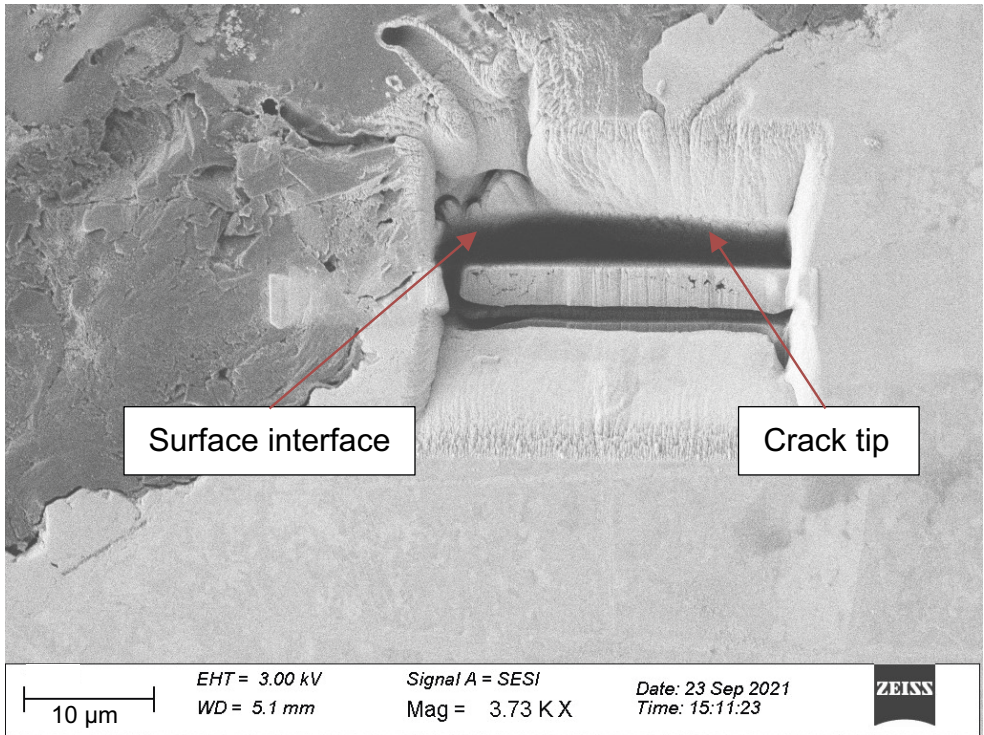

Figure A-3. *SEM image of the lamella produced from specimen #3 before lifting.*
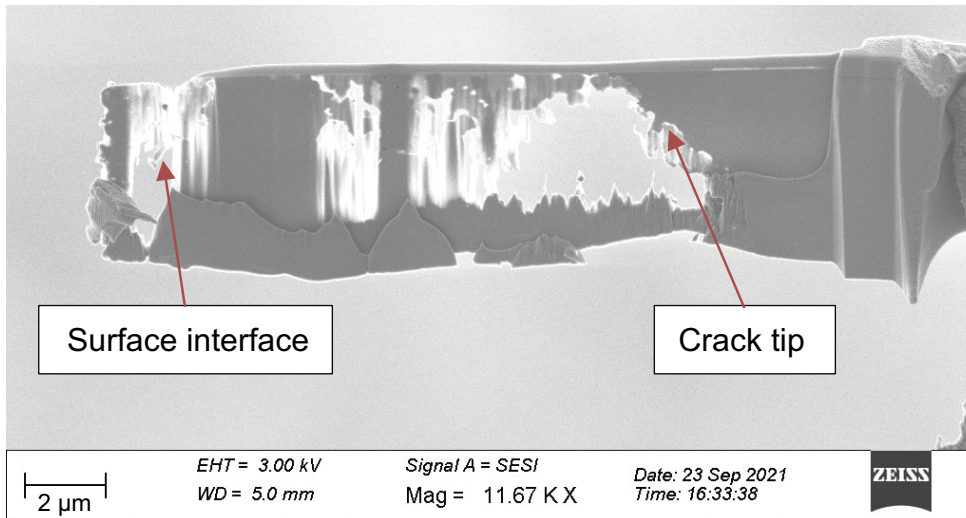
Figure A-4. *SEM image of lamella from Rod #3. The left side corresponds to the surface interface between metallic copper and corrosion products, while the right side corresponds to the crack tip interface. Part of the corrosion products fell off from the lamella during preparation.*
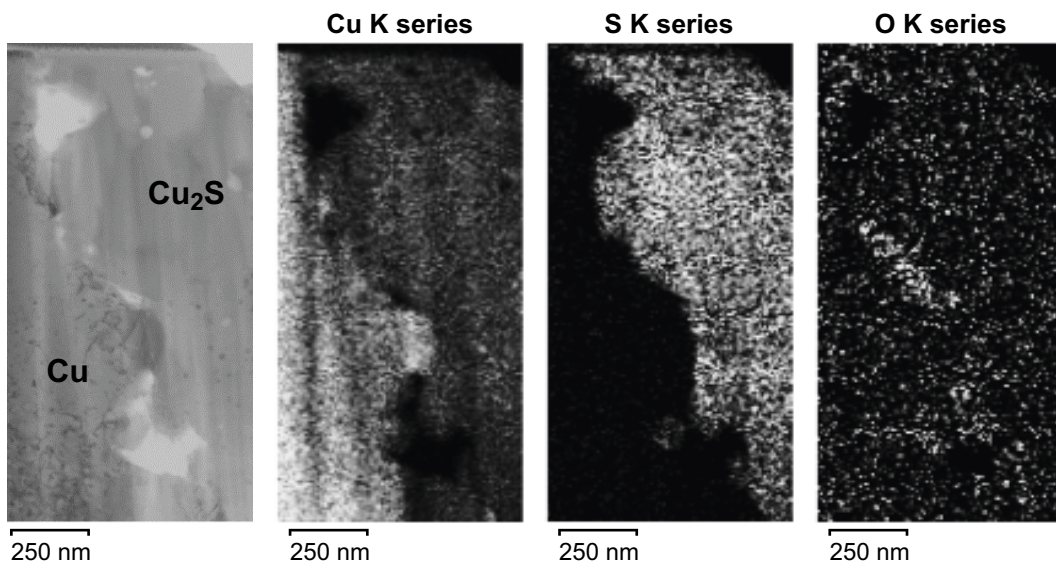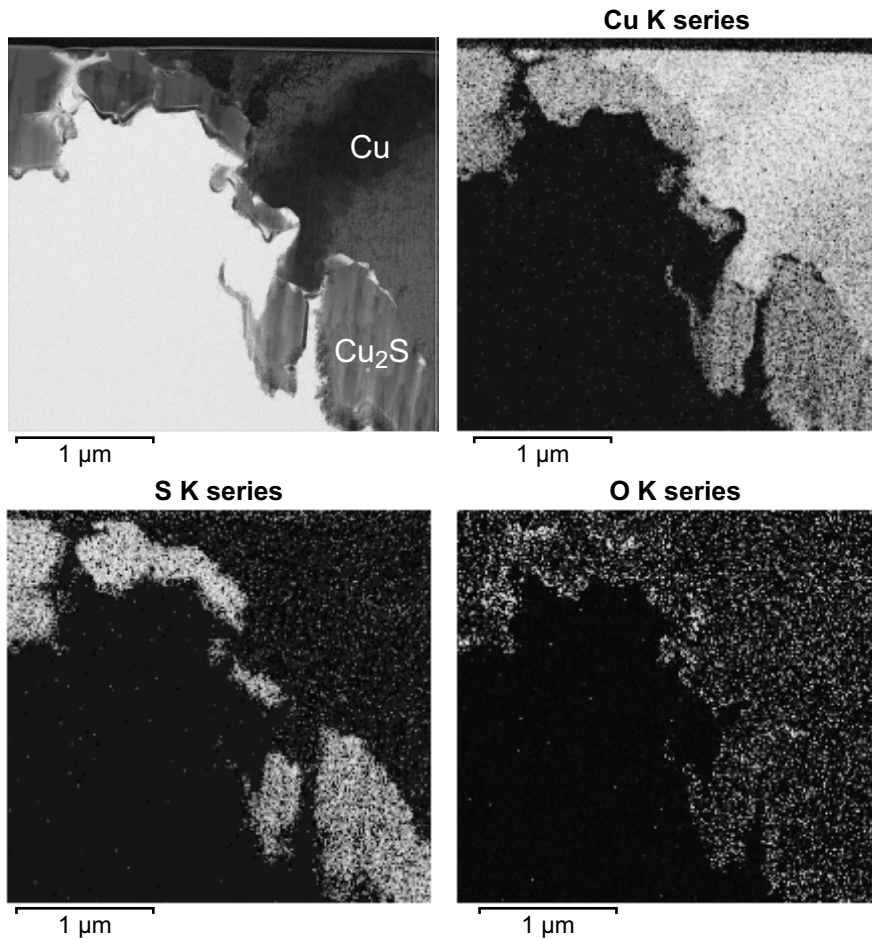

Figure A-5. *STEM image of the surface interface between metallic copper and corrosion products (leftmost image). EDS maps of Cu, S and O species. Only small amounts of oxygen were observed directly in the interface.*

250 nm
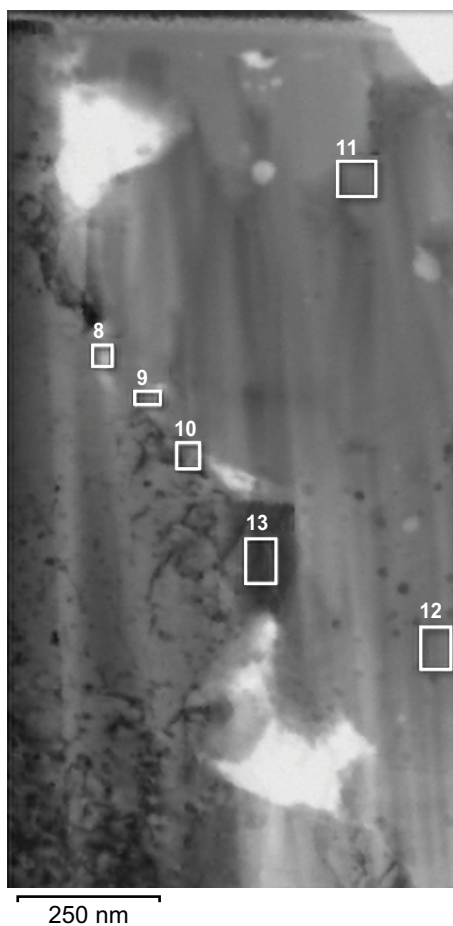
Spectrum label	O	Si	S	Cu	Total
8	32.6	0.0	12.0	55.4	100.0
9	17.7	0.0	0.0	82.3	100.0
10	31.7	1.6	2.5	64.2	100.0
11	7.5	0.0	30.3	62.3	100.0
12	0.0	0.0	31.7	68.3	100.0
13	0.0	0.0	0.0	100.0	100.0

Figure A-6. *STEM image of surface interface between metallic copper and corrosion products in feature of Rod #3. The numbers refer to the elemental composition defined in the table, done by EDS and shown in atomic percent. Cu_2S is likely present (spectra label 11 and 12). There were not enough oxides remaining at the surface interface to be able to identify phases using diffraction.*

Cu K series

S K series

O K series

1 µm

Figure A-7. *STEM image of the crack tip in feature of Rod #3 (top left image). EDS maps of Cu, S and O species. Only small amounts of oxygen were observed directly in the interface.*
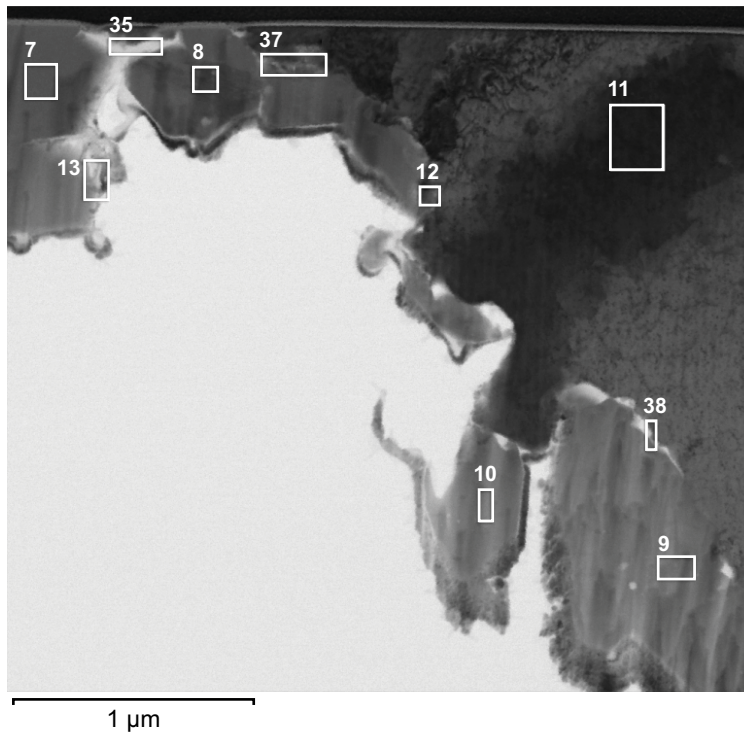
| Spectrum label	O	Si	S	Cu	Total
7	0.0	0.0	33.3	66.7	100.0
8	0.0	0.0	29.0	71.0	100.0
9	0.0	0.0	29.6	70.4	100.0
10	0.0	0.0	31.4	68.6	100.0
11	2.0	0.0	0.0	98.0	100.0
12	25.3	0.0	0.0	74.7	100.0
13	32.5	4.3	12.0	51.3	100.0
35	53.8	0.0	2.9	43.3	100.0
37	13.4	0.0	7.1	79.5	100.0
38	15.4	0.0	9.7	74.9	100.0

Figure A-8. *STEM image of crack tip in feature of Rod #3. The numbers refer to the elemental composition defined in the table, done by EDS and shown in atomic percent. The sulfide present in the crack is likely Cu₂S (spectra 7 to 10). Silicon is likely contamination from the sample preparation process. It is not clear from EDS what kind of oxide is present.*

A2.2   Rod #4 (lamella 1)

One of the lamellae obtained from Rod #4 was lifted at the position shown in Figure A-9. Figures A-10 to A-12 show how the lamella was cut from the rod and the two areas of interest: the surface interface and the crack tip. The interface region appears to have been contaminated during specimen preparation and handling, therefore no results from this area are shown in the report.
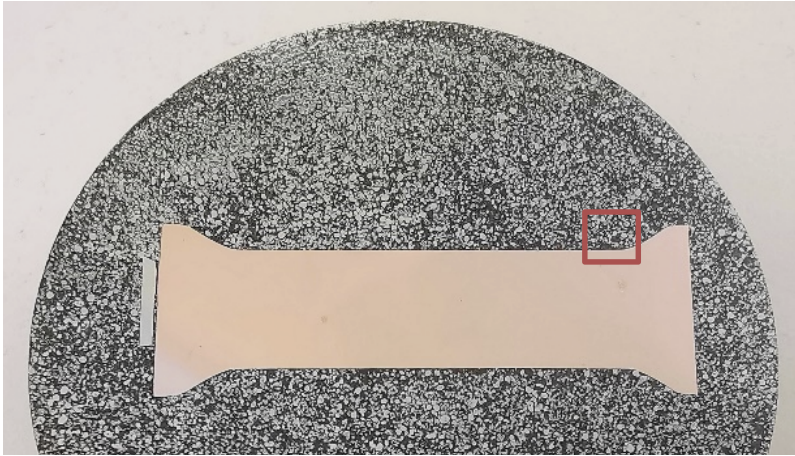
Figure A-9. *Longitudinal cross section of a copper rod mounted in bakelite. The red square shows the approximate location of the selected feature.*
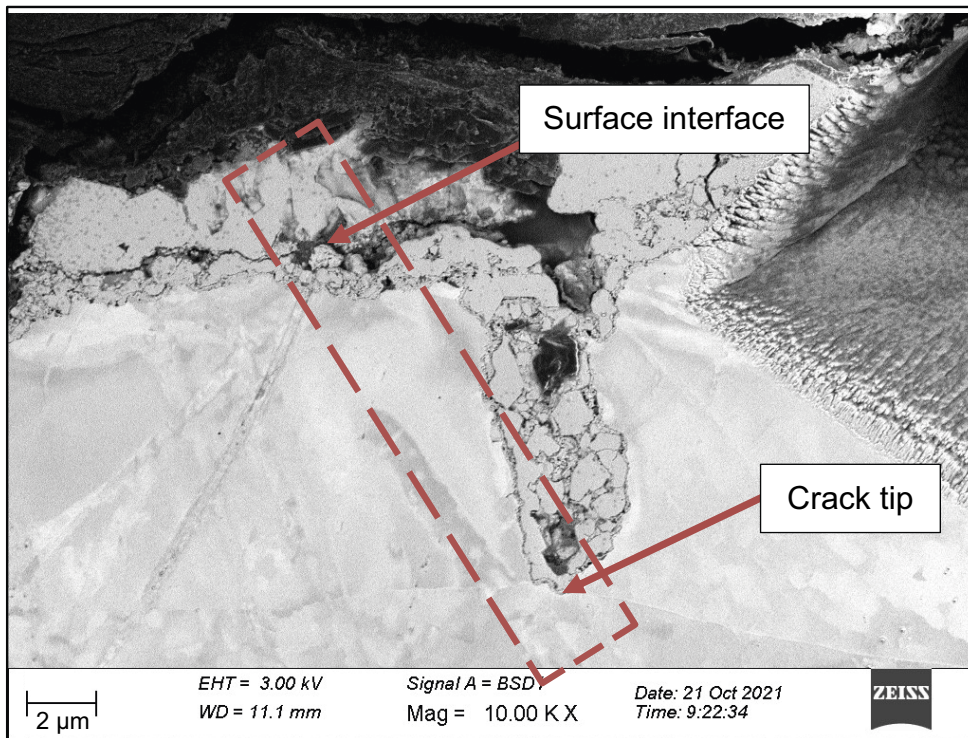
Figure A-10. *SEM image of the selected location for the FIB lamella in the cross section of Rod #4 (red dashed lines represent the approximate site where the lamella was lifted). The right side of the image shows surface damage from a previous unsuccessful attempt to lift out a lamella in another area of the same specimen.*
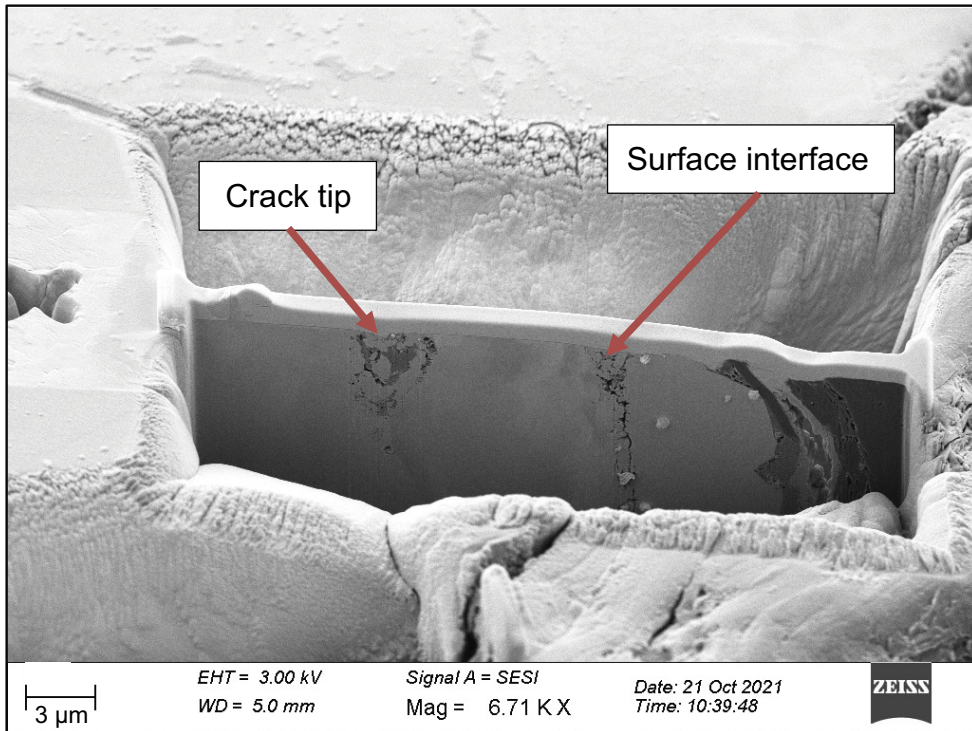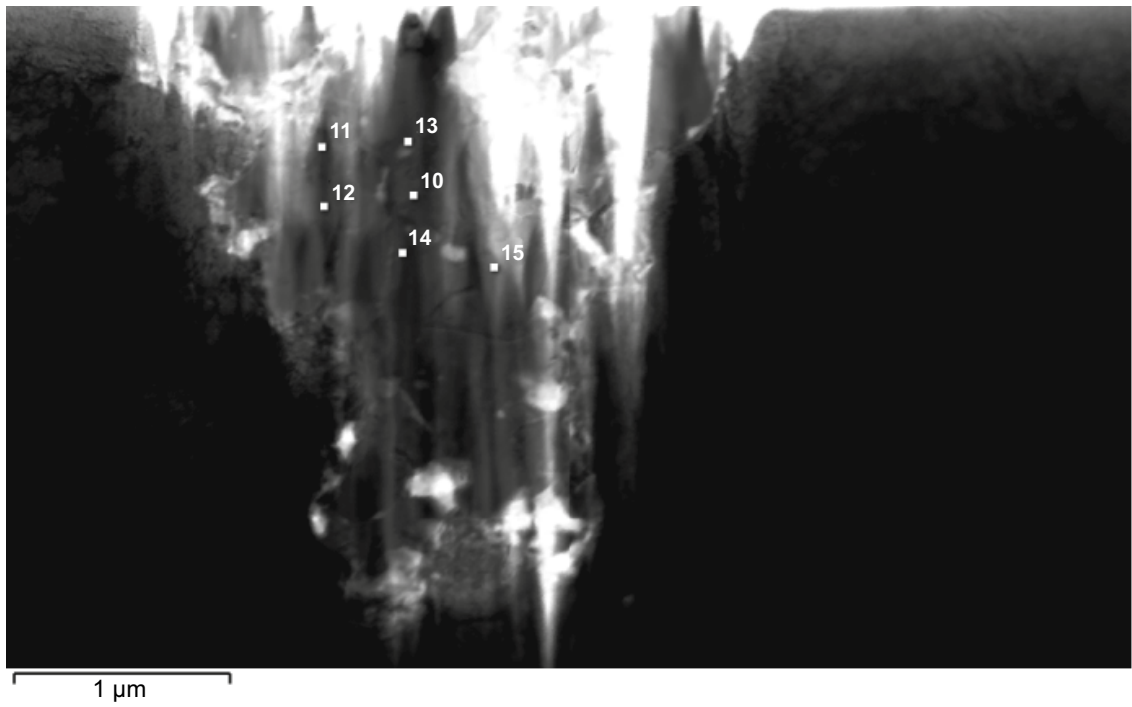
Figure A-11. *SEM image of the lamella produced from Rod #4 before lifting.*

Figure A-12. *High Resolution TEM image of lamella from Rod #4. The left side corresponds to the crack tip interface, while the right side corresponds to the surface interface between metallic copper and corrosion products.*

| Spectrum label	O	Si	S	Fe	Cu	Total
10	4.1	0.2	28.5	0.2	67.0	100.0
11	13.1	0.3	23.5	0.2	62.9	100.0
12	3.1	0.2	31.8	0.2	64.8	100.0
13	1.2	0.0	30.9	0.1	67.8	100.0
14	1.3	0.2	31.3	0.2	67.1	100.0
15	5.3	0.4	31.0	0.1	63.2	100.0

Figure A-13. *STEM image of the crack tip region found in lamella from Rod #4. The numbers in the image correspond to elemental composition referred to in the table (done by EDS and shown in atomic percent).*

A2.3   Rod #4 (lamella 2)

The second lamella obtained from Rod #4 was lifted at the position shown in Figure A-14. Figures A-15 to A-17 show how the lamella was cut from the rod and the two areas of interest: the surface interface and the crack tip.
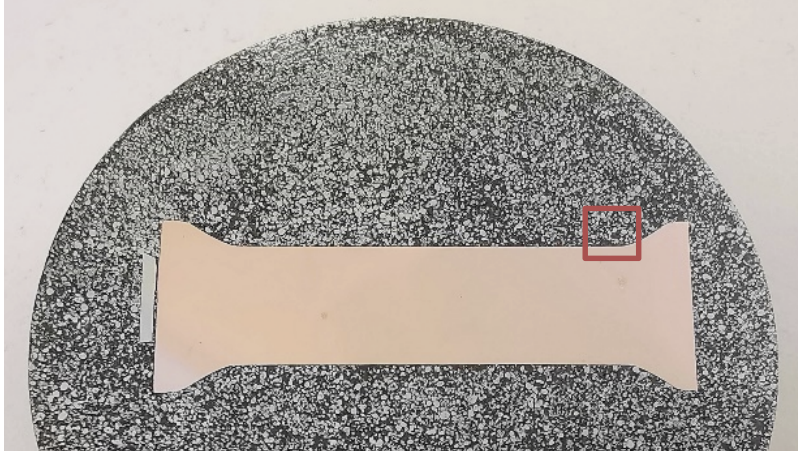

Figure A-14. *Longitudinal cross section of a copper rod mounted in bakelite. The red square shows the approximate location of the selected feature.*
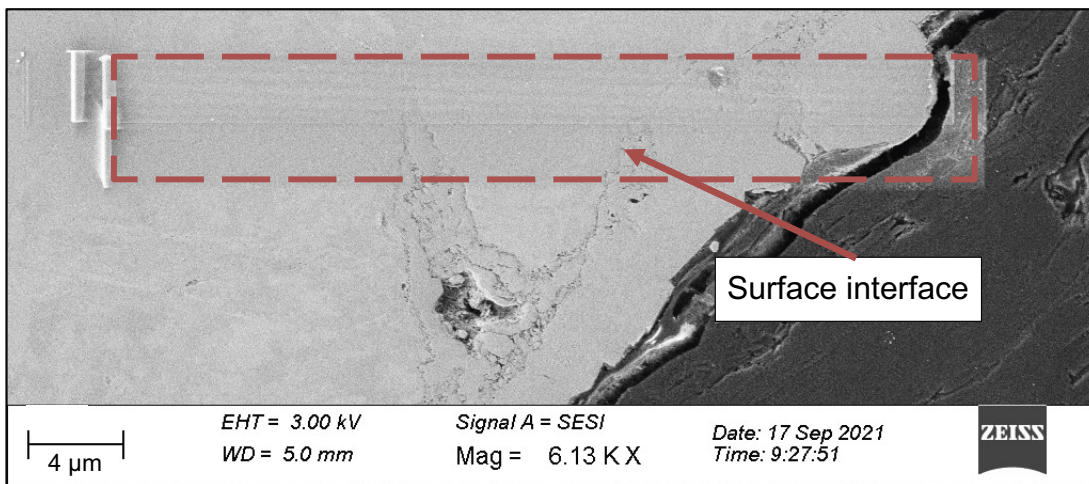

Figure A-15. *image of the selected location for the FIB lamella in the cross section of Rod #4 (red dashed lines represent the approximate site where the lamella was lifted).*
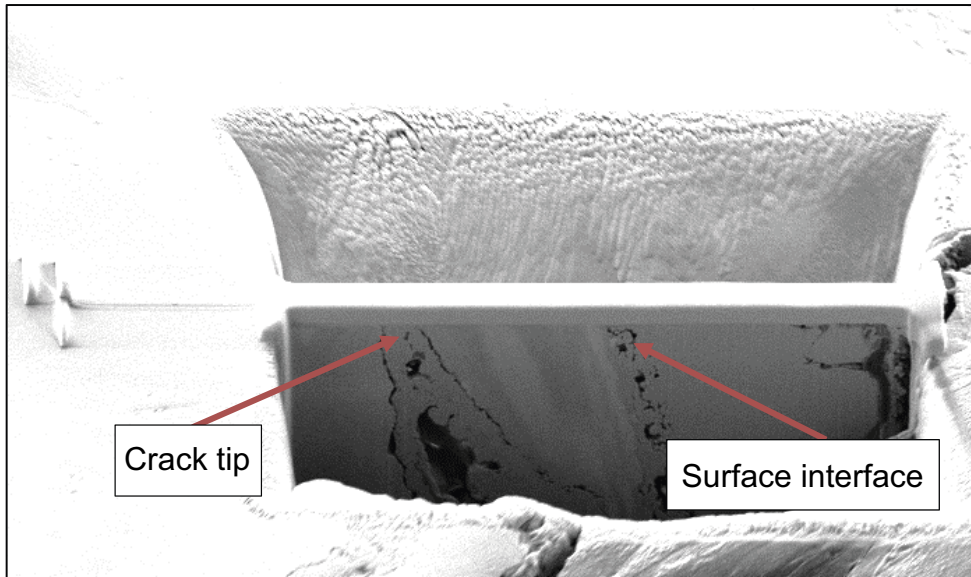
*Figure A-16.* *SEM image of the lamella produced from Rod #4 before lifting.*
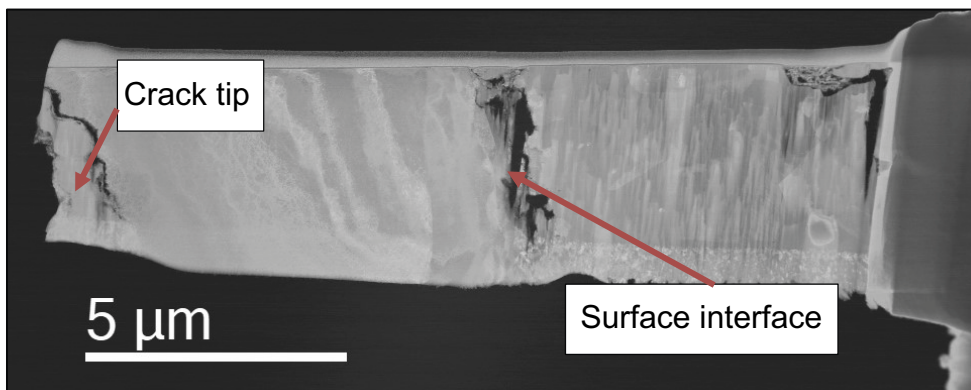
Figure A-17. *High Resolution TEM image of lamella from Rod #4. The left side corresponds to the crack tip interface, while the right side corresponds to the surface interface between metallic copper and corrosion products. The outer part of the crack tip fell off during handling.*
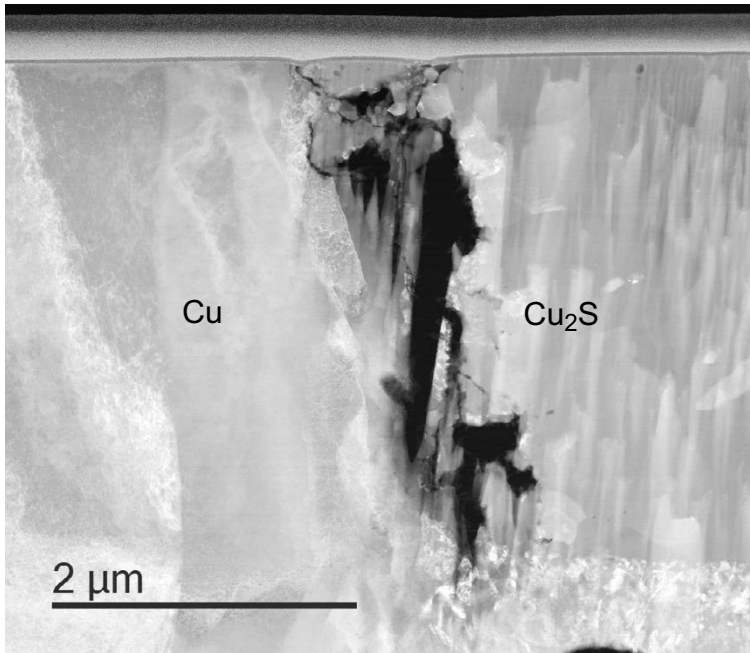
Figure A-18. *High Resolution TEM image of surface interface between metallic copper and corrosion products.*
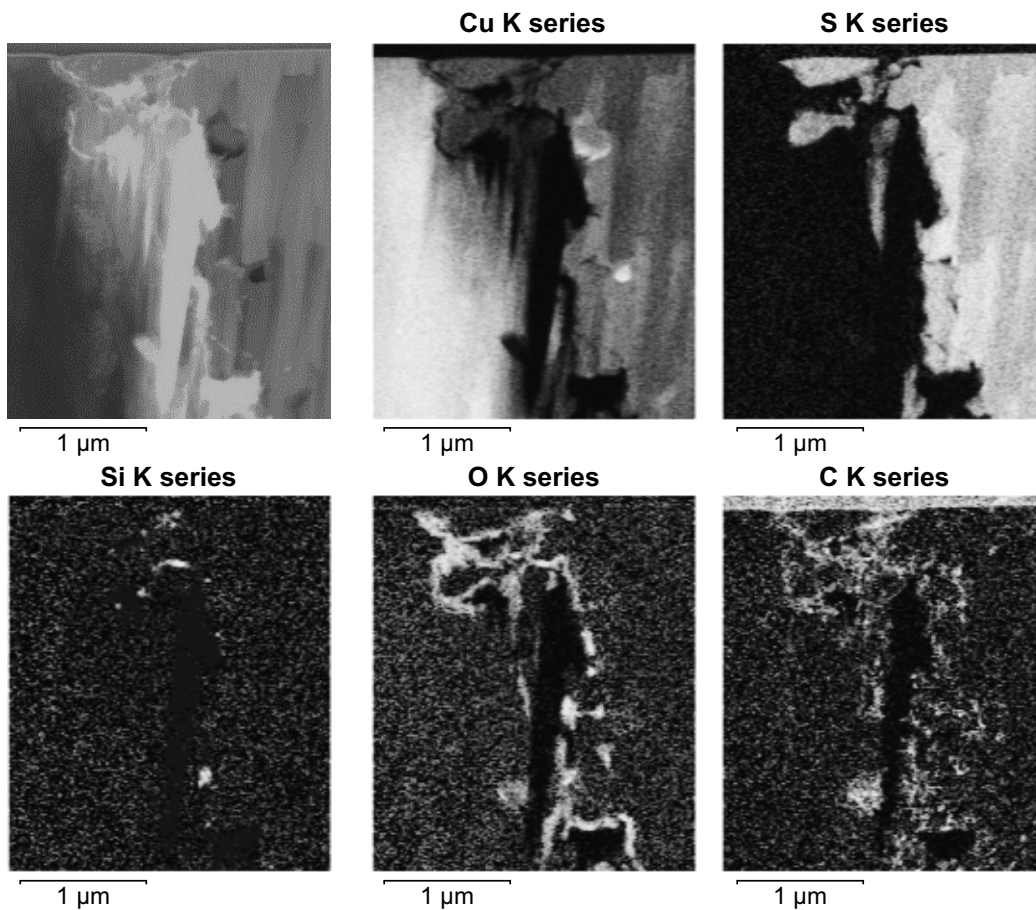

Figure A-19. *STEM image of the surface interface between metallic copper and corrosion products in Rod #4 (top left). EDS maps of Cu, S, Si, O and C species. Si and C species likely to originate from sample preparation.*
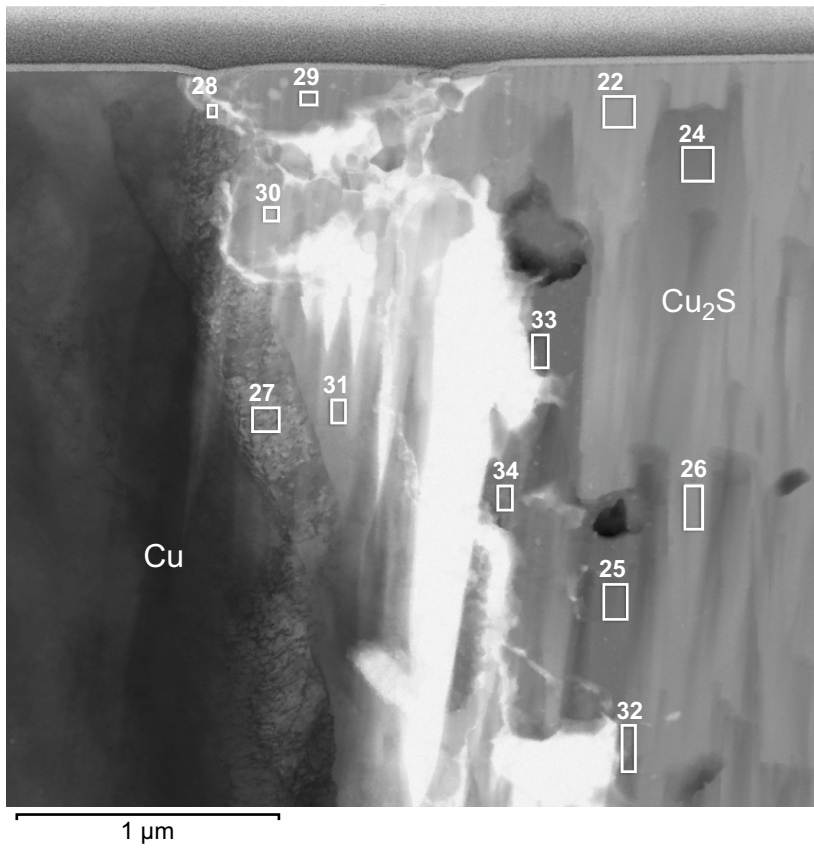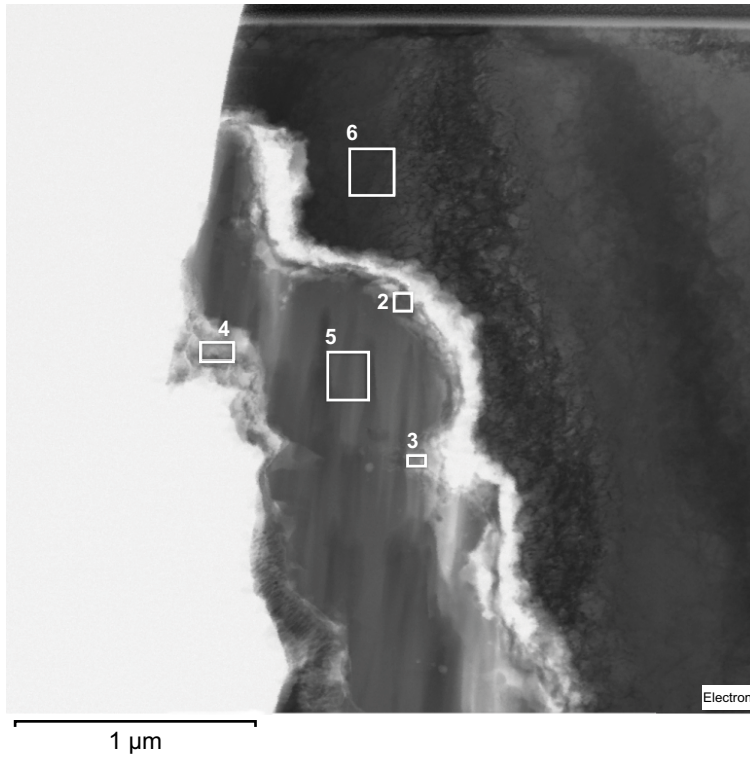
Spectrum label	O	S	Cu	Total
22	3.0	33.2	63.8	100.0
24	2.9	32.6	64.5	100.0
25	1.5	33.5	65.0	100.0
26	0.0	33.3	66.7	100.0
27	0.0	0.0	100.0	100.0
28	36.3	0.0	63.7	100.0
29	0.0	34.1	65.9	100.0
30	0.0	37.0	63.0	100.0
31	5.6	0.0	94.5	100.0
32	30.0	7.9	62.1	100.0
33	26.6	8.4	65.0	100.0
34	27.9	6.6	65.6	100.0

Figure A-20. STEM image of the surface interface between metallic copper and corrosion products in Rod #4. The numbers refer to the elemental composition defined in the table, done by EDS and shown in atomic percent. Sulfide is present at the surface (spectra 22–26, 30, 32–34). Copper oxide found in site 28.

Cu K series

S K series

O K series

1 µm

1 µm

1 µm

1 µm
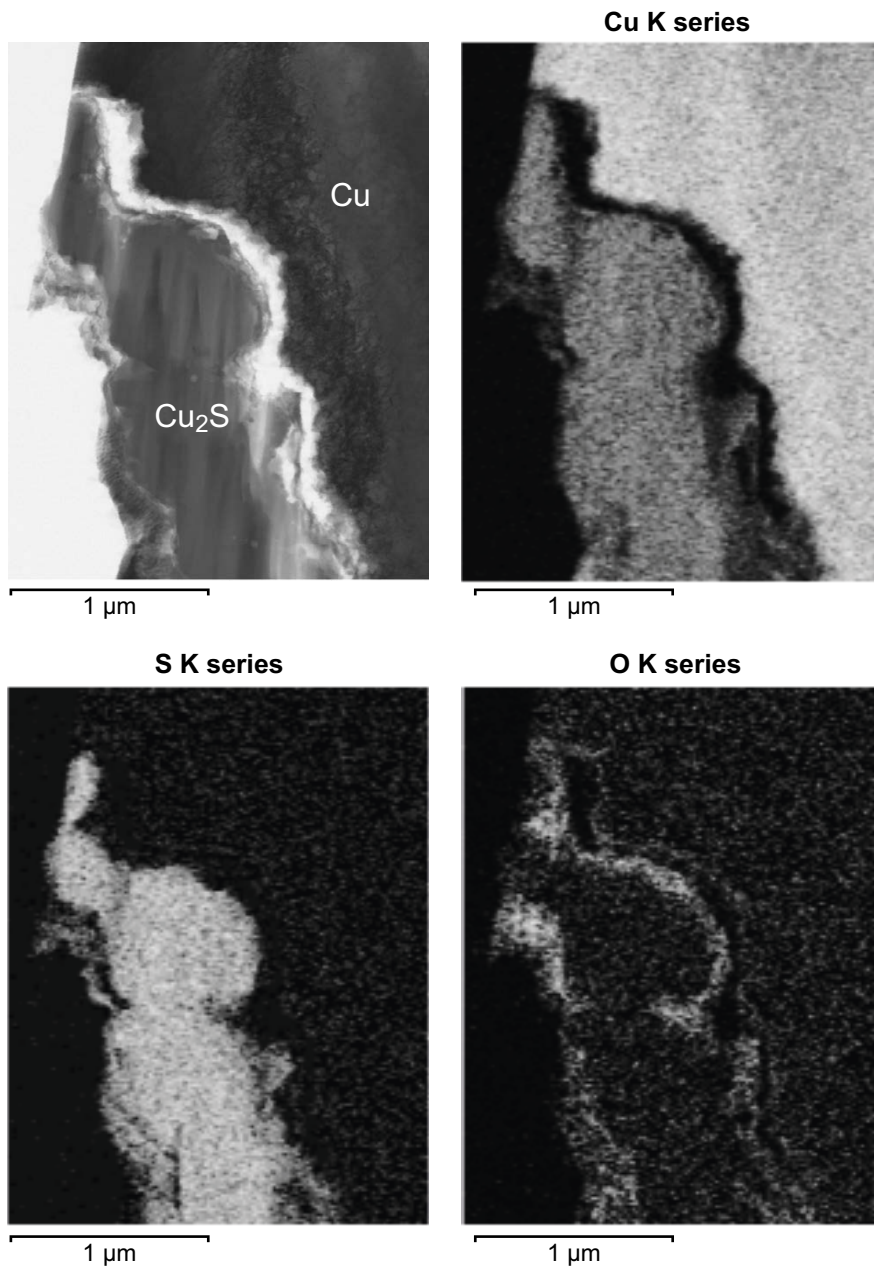
Figure A-21. STEM image of crack tip in Rod #4 (top left). EDS maps of Cu, S a O species.

| Spectrum label	O	Si	S	Cu	Total
2	41.7	0.0	4.3	54.0	100.0
3	49.0	0.0	4.9	46.1	100.0
4	55.0	16.1	7.4	21.6	100.0
5	0.0	0.0	35.8	64.2	100.0
6	0.0	0.0	0.0	100.0	100.0

Figure A-22. *STEM image of crack tip Rod #4. The numbers refer to the elemental composition defined in the table, done by EDS and shown in atomic percent. The oxide (100–200 nm thickness) at the crack tip likely to correspond to CuO (spectra 2–3). Site 5 shows the presence of Cu_2S.*

A3   Conclusions

Sample preparation using FIB allowed a glimpse of the 3D structure of the corrosion attacks. The FFTs images were omitted from the results due to inconclusive phase identification or due to lamella breakage before diffraction data was successfully collected.

This TEM study confirms the presence of trace amounts of oxygen between the major corrosion product, copper sulfide and the copper metal. Local oxygen content up to about 50 % at some sites deep into the apparent cracks was found, balanced mostly by copper. This suggests that the composition is more similar to CuO than to Cu_2O at some sites.

There is no evidence that the oxygen found played any role in the corrosion process, as neither Cu_2O nor CuO are stable compounds under the experimental conditions. The measured corrosion potentials are too low. Cu_2O could conceivably be formed from oxidized sulfur species but the formation of CuO from such a reaction seems highly improbable. For example, one such reaction:

$$S_2O_3^{2-} + H_2O + 8Cu(s) \rightarrow 2Cu_2S(s) + 2Cu_2O(s) + 2OH^- \qquad (A\text{-}1)$$
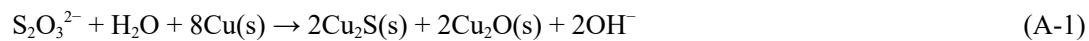
The reasonable explanation of its presence is that the copper-oxygen compounds were formed after the experiments. A possible explanation for higher prevalence of oxygen in deeper crack- or pit-like features than outside these corrosion attacks, is the longer time required for remaining water to evaporate. A longer wet time in the atmosphere allowed more oxygen to react with metallic copper and with amorphous copper sulfides.

SKB is responsible for managing spent nuclear fuel and radioactive waste produced by the Swedish nuclear power plants such that man and the environment are protected in the near and distant future.

skb.se